

Seasonal Distributions of Global Ocean Chlorophyll and Nutrients: Analysis with a Coupled Ocean General Circulation, Biogeochemical, and Radiative Model

Watson W. Gregg
Laboratory for Hydrospheric Processes
NASA/ Goddard Space Flight Center
Greenbelt, MD 20771

Submitted to Journal of Geophysical Research, 1999

Abstract

A coupled general ocean circulation, biogeochemical, and radiative model was constructed to evaluate and understand the nature of seasonal variability of chlorophyll and nutrients in the global oceans. The model is driven by climatological meteorological conditions, cloud cover, and sea surface temperature. Biogeochemical processes in the model are determined from the influences of circulation and turbulence dynamics, irradiance availability, and the interactions among three functional phytoplankton groups (diatoms, chorophytes, and picoplankton) and three nutrient groups (nitrate, ammonium, and silicate). Phytoplankton groups are initialized as homogeneous fields horizontally and vertically, and allowed to distribute themselves according to the prevailing conditions.

Basin-scale model chlorophyll results are in very good agreement with CZCS pigments in virtually every global region. Seasonal variability observed in the CZCS is also well represented in the model. Synoptic scale (100-1000 km) comparisons of imagery are also in good conformance, although occasional departures are apparent. Agreement of nitrate distributions with *in situ* data is even better, including seasonal dynamics, except for the equatorial Atlantic. The good agreement of the model with satellite and *in situ* data sources indicates that the model dynamics realistically simulate phytoplankton and nutrient dynamics on synoptic scales. This is especially true given that initial conditions are homogenous chlorophyll fields.

The success of the model in producing a reasonable representation of chlorophyll and nutrient distributions and seasonal variability in the global oceans is attributed to the application of a generalized, processes-driven approach as opposed to regional parameterization, and the existence of multiple phytoplankton groups with different physiological and physical properties. These factors enable the model to simultaneously represent the great diversity of physical, biological, chemical, and radiative environments encountered in the global oceans.

Introduction

The seasonal cycle is one of the dominant signals in global ocean chlorophyll and nutrient distributions. Although solar radiation and the time-lagged heat cycle are ultimately responsible for the seasonal cycle, a complex set of physical, biological, chemical, and radiative processes determine the nature of the variability. A complete observation of these processes and their interactions on a global scale is beyond our capabilities, because of the vast expanse of the oceans, despite the advent of routine spaceborne observational programs. However, numerical models of fundamental

processes coupled with large scale observations, can help identify and elucidate the specific causes, magnitudes, and nature of seasonal variability.

It is a challenge to represent the wide diversity of the global oceans. Other attempts, e.g. Longhurst (1995); Sathyendranath et al. (1995); Platt et al. (1991), subdivided the oceans into functional regions, or provinces. These provinces are distinguished from one another in several key physical, biological and chemical conditions. While this type of analysis provides a representation of the diversity of global ecosystems, it suffers from the influences of dynamical processes. Seasonal variability can produce changes in the processes within these provinces, sometimes to the extent that they are no longer functionally coherent. In a dynamical representation of the global oceans, a phytoplankton particle can move from location to location. In the province classification method, this phytoplankton particle may be required to change its inherent characteristics upon entering the new province.

In this coupled, interactive model of circulation, biological, chemical, and radiative processes, regional characterizations are avoided. This representation attempts to simulate the wide range of global phytoplankton abundances and diversity using common processes, that are modified by the characteristics of the prevailing physical environment. Thus the model is general. While this approach may result in some lack of accuracy in the final global representations, we gain an understanding of the fundamental processes causing the distributions of phytoplankton. Such a representation naturally leads to a reduction of parameterizations required as well, and focuses the problem on the influence of processes.

Essentially, a generalized parameter is defined that is in agreement with the realm of typical ocean conditions. Naturally occurring processes are sought that affect that representation in different physical conditions, and then the environmental conditions are allowed to dictate the specific response. For example, we define a gross sinking rate according to a typical phytoplankton diameter and under typical temperatures and viscosities using Stokes Law. Then sinking rates are allowed to change according to the different viscosities encountered in the global ocean.

The key features of the coupled model are:

- 1) Global scale, three-dimensional, with interactive and general hydrodynamical, biological, chemical, and radiative transfer processes
- 2) Multiple phytoplankton groups, which differ in growth rates, sinking rates, and optical properties
- 3) 3 photoadaptation states, corresponding with 3 carbon:chlorophyll states, based on the prevailing irradiance
- 4) Complete spectral and radiative treatment including the optical properties of a variable atmosphere and ocean, and accounting for the spectral as well as directional properties of irradiance and radiance transmittance with explicit cloud radiative transfer modeling
- 5) Emphasis on processes, not parameters
- 6) No regional tuning – explicit common global processes

This effort builds on previous work coupling three-dimensional physical, biological, chemical, and radiative processes in selected regions (e.g., Walsh et al., 1999; Gregg and Walsh, 1992) in an attempt to construct a reasonable representation of global chlorophyll and nutrient dynamics, the processes affecting them, and their seasonal variability. Since seasonal variability is the focus, a climatological representation of atmospheric and oceanic forcing conditions is employed. Results

are compared to observations where available. The focus here is on the surface layer only, because of the availability of remote sensing data for validation. Additionally, this paper emphasizes the coupling between the circulation and biogeochemical components of the model, although the radiative model is briefly described. Further analysis of the interactions of the radiative coupling are discussed elsewhere (Gregg, 1999).

Methods

This effort assumes that, to first order, the large scale (synoptic scale; 100-1000 km), low frequency (subtidal) features of global seasonal biogeochemical distributions may be described by a system of equations comprising mixing, advection, sinking, growth of phytoplankton as a function of light, temperature, and nutrient availability, and death by ingestion and senescence. This assumption leads to a set of coupled, partial differential equations called the governing equations of the simulation analysis

$$\frac{\partial}{\partial t} C_i = \nabla(A\nabla C_i) - \nabla \bullet \mathbf{V} C_i - \nabla \bullet (\mathbf{w}_s)_i C_i + \mu_i C_i - gH - sC_i \quad (1)$$

$$\frac{\partial}{\partial t} N_k = \nabla(A\nabla N_k) - \nabla \bullet \mathbf{V} N_k - b_k \sum_i C_i \mu_i + [b_k \gamma_k g \sum_i C_i] H + b_k \epsilon_k s \sum_i C_i + b_k \epsilon_k [n_1 H + n_2 H^2] + b_k r_k D \quad (2)$$

$$\frac{\partial}{\partial t} H = \nabla(A\nabla H) - \nabla \bullet \mathbf{V} H + [\sum_k (1 - \gamma_k) g \sum_i C_i] H - n_1 H - n_2 H^2 \quad (3)$$

$$\frac{\partial}{\partial t} D = -\nabla \bullet \mathbf{w}_d D - \sum_k r_k D + \sum_k (1 - \epsilon_k) s \sum_i C_i + \sum_k (1 - \epsilon_k) [n_1 H + n_2 H^2] \quad (4)$$

where the subscripts k and i denote the existence of discrete quantities of nutrients (N, as nitrate, ammonium, and silicate) and chlorophyll (C, as diatoms, chlorophytes, and picoplankton), and bold denotes a vector quantity. H represents herbivores and D represents detritus. Other symbols are defined in Table 1.

The first term on the right hand side in Eqs. 1 and 2 represents diffusion, the second represents advection, the third in Eq. 1 only is sinking (which does not apply to dissolved nutrients, and also goes to zero in the horizontal), and the remaining terms are the biological processes terms. Explicit advection and diffusion processes are ignored for detritus to reduce the computational burden. However, advection and diffusion processes become represented when detritus remineralizes back to nutrient form (Eq. 2).

To solve this set of equations, one requires three separate models to obtain numerical values for the variables. A circulation model computes advection, mixing, and sinking, and thus determines the time-dependent horizontal and vertical motions of phytoplankton, nutrients, herbivores, and detritus. A biogeochemical processes model derives growth of phytoplankton resulting from the calculated light field, temperature, and nutrient assimilation, and death resulting from grazing and other ingestion as well as senescence. It also determines the fate of nutrients, herbivores, and detritus as related to the growth and abundance of chlorophyll. The radiative model determines the availability of light at the surface and in the water column. A diagrammatic representation of the fully coupled dynamic model illustrates the complex interactions among the three major components: a global hydrodynamical General Circulation Model (GCM), a general biogeochemical processes model, and a general radiative model (Figure 1). Although there are several nominal outputs of the coupled model, e.g., spectral radiance, primary production, and biogeochemical constituent distributions, only the latter are considered here.

General Circulation Model

The GCM is a reduced gravity representation of circulation fields, and is nearly global in scale, extending from near the South Pole to 72° N, in increments of 2/3° latitude and 1 1/4° longitude (Schopf and Lough, 1995). Only ocean areas with depths exceeding 200 m are active. The model contains multiple vertical layers, in quasi-isopycnal coordinates, with the deepest interface in the model at a mean depth of 2800 meters. The number of layers is a choice between vertical resolution and computational expense. A 14-layer version provides an adequate representation of surface and upper ocean hydrodynamics at reasonable computational cost. The surface layer represents the upper mixed layer, then there are several layers of fixed thickness to prevent outcropping, and the remaining layer depths are based on the density distribution. The water beneath the deepest interface is assumed to sustain no pressure gradients (i.e., a reduced gravity approximation). Vertical mixing is Richardson number-dependent, following Pacanowski and Philander (1981), and is performed in a time splitting mode, occurring every 12 hours in contrast to the 0.5 hour Δt of the advective processes. Experiments at shorter Δt (6 h) indicated little discernible effect. Convection is parameterized as vertical mixing at large Richardson number. The model uses a midpoint leap frog method to advance in time (Roache, 1982) and is driven by monthly climatologies of wind stresses, heat fluxes, and sea surface temperature (da Silva, 1994). The surface layer temperature of the model relaxes to sea surface temperature, computed daily. The model is initialized by temperature and salinity from climatologies (Levitus and Boyer, 1994; Levitus, et al., 1994), and run for 5 years to achieve steady state.

General Biogeochemical Model

The biogeochemical model utilizes the circulation fields and the vertical mixing processes to produce horizontal and vertical distributions of constituents. The biogeochemical constituents are non-conservative, of course, and have their own local dynamical processes (Figure 2). There are 3 phytoplankton groups, which differ in maximum growth rates, sinking rates, nutrient requirements, and optical properties to help us represent the extreme variety of physical environments encountered in a global model (Figure 3). Three nutrient groups are included to simulate "new" use of nitrogen (Dugdale and Goering, 1967; Eppley and Peterson, 1979) represented by nitrate, regenerated

nitrogen represented by ammonium, and silicate as an additional requirement of diatoms. Phytoplankton are ingested by a separate herbivore component, which also contributes to the ammonium field through excretion. Death by senescence contributes a small portion to the ammonium pool, but mostly to the detrital pool, which is ultimately remineralized back to original nutrients. The biogeochemical model has 8 state variables in the fully coupled model.

Phytoplankton growth is a function of light and nutrient availability, and temperature. It is evaluated at the minimum value for light and nutrients, to represent the effects of a single limiting factor (Pribble et al. 1994) rather than multiplicative factors (e.g., Gregg and Walsh, 1992), and adjusted by temperature

$$\mu = \min[\mu(E_t), \mu(\text{NO}_3), \mu(\text{NH}_4), \mu(\text{SiO}_3)] \mu(T) \quad (5)$$

where μ is the total specific growth rate (d^{-1}) of phytoplankton, E_t is the total irradiance at depth (μM quanta $\text{m}^{-2} \text{s}^{-1}$), and NO_3 , NH_4 , and SiO_3 are the nitrate, ammonium, and silicate concentrations, respectively (μM). The total specific growth rate is modified by temperature according to Eppley (1972)

$$\mu(T)_i = (0.851\alpha 1.066^T)\beta_i \quad (6)$$

where α is a factor to convert to units of d^{-1} (instead of doublings d^{-1}) and to adjust for a 12-hour photoperiod, and β is an additional adjustment is used for the picoplankton component that reduces their growth rate in cold water ($<15^\circ\text{C}$)

$$\beta_3 = 0.02941T + 0.5582 \quad (7)$$

This effect produces a nearly constant Δ maximum growth rate with diatoms at low temperatures. Temperature effects are evaluated once per day for computational convenience.

Phytoplankton growth as a function of light is approximated using Kiefer and Mitchell (1983)

$$\mu(E_t) = \frac{\mu_m E_t}{(E_t + K_E)} \quad (8)$$

where μ is the specific growth rate (d^{-1}), the subscript m indicates the maximum growth rate, and K_E is the irradiance at which $\mu = 1/2\mu_m$. K_E is related to the commonly reported light saturation parameter, I_k , by the factor 0.5. Respiration is ignored in this model. Expressions for μ_m and K_E are phytoplankton group-dependent, and thus contribute to the overall group characterizations. K_E is additionally dependent on the prevailing irradiance, to simulate photoadaptation. We divide photoadaptation into 3 classes: 50, 150 and 200 (μM quanta $\text{m}^{-2} \text{s}^{-1}$). We compute the mean irradiance during daylight hours, and then classify the phytoplankton photoadaptive state accordingly. This calculation is only performed once per day to simulate a delayed photoadaptation response.

Correspondingly, carbon:chlorophyll ratios are related directly to the photoadaptation state. This simulates the behavior of phytoplankton to synthesize chlorophyll preferentially in low light conditions, to enable more efficient photon capture. These three C:chl states are 25, 50 and 80.

The C:chl classification is important for evaluating primary production, but more immediately, determining the nutrient:chlorophyll ratios, which are computed assuming the Redfield elemental balances

$$b = (C:chl)/79.5 \quad (9)$$

Growth limitation is also nutrient-dependent, and follows the Monod uptake kinetics model. All phytoplankton groups are limited by nitrogen, as nitrate and ammonium, and diatoms are additionally limited by silicate concentrations. Ammonium is preferentially utilized over nitrate, following the formulation of Gregg and Walsh (1992). Half-saturation constants are group-independent (Table 1). The picoplankton component possesses a modest ability to fix nitrogen from the water column, as is observed in *Trichodesmium* spp. (Carpenter and Romans, 1991). The nitrogen fixation is expressed as 0.001 the light-limited growth rate, and only applies when nitrate availability is $< 1 \mu\text{M}$. The fixed nitrogen is outgassed by the detrital component to prevent nitrogen accumulation in the model domain.

Typical sinking rates for the phytoplankton groups (Figure 3) are computed by declaring representative individual sizes, and then using Stokes Law under typical oceanic conditions, e.g.,

$$w_s = \frac{2g(\rho_i - \rho)}{9\nu\rho} r^2 \quad (10)$$

where w_s is the sinking rate (m d^{-1}), g is gravitational acceleration (m s^{-2}), ρ_i is the density of the phytoplankton component, ρ is the density of seawater, ν is the viscosity of seawater, and r is the particle radius (Csanady, 1986). Modification of this rate can occur under circumstances deviating from the typical conditions, such as in extremely cold water where viscosities are large. Using Stokes Law, this effect is parameterized in terms of temperature, normalizing to the sinking rate at 20°C

$$w_s(T) = w_s(20)[0.451 + 0.0178T] \quad (11)$$

Simulation of grazing by the herbivore component is based on McGillicuddy et al. (1995).

$$g(T) = R(T)[1 - \exp(-\Lambda \sum C_i)] \quad (12)$$

A temperature-dependence in grazing is enforced,

$$A = 1.066^{1.4T} + 4 \quad (13)$$

which is normalized by the rate at 20°C

$$R(T) = R_m 1.1 A(T) / A(20^\circ) \quad (14)$$

Again temperature effects are evaluated daily. Note the functional similarity between this expression and the phytoplankton growth rate dependence. This temperature-dependence in grazing enables us to keep growth and grazing in approximate balance over the diversity of environments in the global oceans.

There are no refuge populations in the model (e.g., Bissett et al., 1999). Phytoplankton groups are allowed to become extinct if conditions to support their survival do not exist.

General Radiative Transfer Model

Rigorous radiative transfer calculations are necessary to provide the underwater irradiance fields to drive growth of the phytoplankton groups, accounting for the absorption of light by water and other optically active constituents. The model contains a treatment of the spectral and directional properties of radiative transfer in the oceans, and explicitly accounts for clouds. It contains an optical characterization of atmospheric and in-water optical constituents. The atmospheric radiative model is based on the Gregg and Carder (1990) spectral model for clear skies, and relies on Slingo (1989) for spectral cloud transmittance. It requires external monthly climatologies of cloud properties (cloud cover, optical thickness, and liquid water path), surface pressure, wind speeds, relative humidity, and precipitable water. Computations are made only for the spectral range 350-700 nm (photosynthetically available radiation, or PAR), since the model is used to drive phytoplankton growth only, and only every 2 h to provide diurnal variability at an acceptable computational cost.

Oceanic radiative properties are driven by water absorption and scattering, and the optical properties of the phytoplankton groups. Three irradiance paths are enabled: a downwelling direct path, a downwelling diffuse (scattered) path, and an upwelling diffuse path (Gregg, 1999). All oceanic radiative calculations include the spectral nature of the irradiance. The influences of the radiative model are not discussed in the present paper, which focuses on the interactions among the biogeochemical components and the resulting distributions.

Model Initialization

The model is initialized with annual climatologies for nitrate and silicate from Conkright et al., 1994a. The remaining biological/chemical variables are set to constant values: 0.5 μM ammonium, and 0.05 mg m^{-3} for each of the phytoplankton groups. The biogeochemical constituents approach steady state after 2 years, which provides one complete seasonal cycle in every region. All analyses in this paper are for the fourth year of simulation, which very nearly mirrors the third year, suggesting that steady state has been reached.

Analyses emphasize comparisons with Coastal Zone Color Scanner (CZCS) pigment data, which at present are the only source of climatology, given the recentness of the Sea-viewing Wide Field-of-view Sensor (SeaWiFS) and the abnormal conditions that have persisted since its launch (El Niño and La Niña). The comparisons are regional basin scale, which exhibit the overall performance of the model, and direct image-to-image comparisons which are used to evaluate synoptic scale aspects of the model as compared to the CZCS. Regions are defined as in [Conkright et al., 1994b, 1998a]:

Antarctic is defined as southward of -40° latitude, the North Pacific and Atlantic Oceans are northward of 40° , and equatorial regions are bounded by -10° and 10° . Comparisons are also made of seasonal nitrate climatologies from the National Oceanographic Data Center (NODC)/Ocean Climate Laboratory (OCL) archives (Conkright et al., 1998b; 1998c; 1998d).

Results and Discussion

Seasonal Trends in Chlorophyll: Basin Scale Means and Comparisons with CZCS

A regional comparison of the model-generated chlorophyll after 4 years from initialization with CZCS pigment exhibits a large degree of correspondence in seasonal cycles (Figures 4-6). This is true for virtually all ocean regions globally.

The North Pacific and Atlantic show a pronounced spring bloom peaking near the boreal summer solstice (Figure 4). In the North Pacific, the magnitude of the bloom predicted by the model is larger than that observed by the CZCS, but within the standard deviation. The timing and magnitude of the North Atlantic spring bloom is well-represented by the model. In both regions the CZCS indicates that the elevated chlorophyll biomass extends well into autumn, while the model predicts a rather sharp die-off, especially in the North Pacific. The North Pacific actually indicates a boreal autumn bloom, that the model does not. In the model, these regions are characterized by large changes in mixed layer depth, and a large variability in irradiance, due to the seasonal variability in solar zenith angle and day length. This gives rise to mixed layer deepening in winter that, coupled with low irradiance, prevents significant phytoplankton growth. Turbulence and convective overturn provide nutrients that cannot be utilized. Upon the arrival of spring/summer, solar irradiance increases and increased surface heating leads to shallower mixed layer depths. This provides the conditions for an extensive phytoplankton bloom, the dynamics of which are represented in the model, and which is responding properly to surface conditions. The late fall bloom in the CZCS, occurring in October-November, could be the result of mixed layer deepening and injection of nutrients, but is more likely due to poor sampling. Northerly portions of both the North Pacific and Atlantic are poorly sampled this time of year, with the only sampling occurring in the southern portions of the basins. The result is a biased mean pigment, since the low pigment concentrations in the northern portions are underrepresented. This is especially true in the North Atlantic. This is a major advantage of realistic numerical model simulations – the ability to produce estimates of chlorophyll under conditions precluding sampling from satellite, such as low light levels. Still, sampled portions suggest higher values in the CZCS than produced by the model. Either death/ingestion/sinking losses are overestimated in the model for this time of year, or errors in the CZCS due to large solar zenith angles are occurring, or a combination.

The model also exhibits good agreement with the North Central Pacific and Atlantic gyres regions, with overall reduced total abundances (mean value near 0.1 mg m^{-3} compared to about 0.5 mg m^{-3} in the sub-polar regions; Figure 4). There is also the appearance of a late winter biomass maximum, occurring in early March. Both the model and CZCS exhibit generally elevated values in winter and depressed values in mid-to-late summer. The late winter maximum is produced in the model from mixed layer deepening (from 10m in August to about 75-100m in December/January), and injection of previously depleted nutrients into depths where there is still sufficient irradiance to produce growth. The deep mixed layer prevents substantial growth to due a reduction in the average

irradiance experienced by phytoplankton. Shallowing of the mixed layer in spring leads to rapid depletion of available nutrients, and a decline in phytoplankton abundances throughout the summer.

Seasonal variability in the tropics is generally suppressed relative to other global regions (Figure 5). The maximum range of variability in the equatorial Indian, Pacific, and Atlantic oceans is only about 0.1 mg m^{-3} . This low range of seasonal variability is well-represented by the model. Even the small maxima and minima in the equatorial Indian and Atlantic Oceans appear to be in correspondence with CZCS pigment. The seasonal variability of the North Indian in the model also appears to be in agreement with the CZCS, with maxima corresponding to the southwest monsoon in August and the less vigorous northeast monsoon in winter. However, the model appears to vastly underestimate the magnitude of the southwest monsoon, especially at the peak in August. The model also appears to underestimate the magnitude of the tropical Pacific pigment concentrations.

The model appears to capture the strong seasonal signal in the North Indian Ocean/Arabian Sea region. However, the model is not as adept in matching magnitudes of the chlorophyll concentrations. The North Indian August mean pigment in the CZCS is the single largest monthly mean recorded in any region in the entire CZCS record. Large chlorophyll concentrations are expected here this time of year, since it corresponds to the peak of the southwest monsoon. Winds during this time of year can exceed 12 m s^{-1} as a monthly mean, which drives vigorous upwelling, nutrient availability, and associated large phytoplankton growth. These dynamics are well-represented in the model, but associated with the strong winds is thick cloud cover (exceeding 80% as a monthly mean, with cloud optical thickness of 4 or more), which in the model tends to suppress vigorous growth. The less vigorous northeast monsoon is also captured by the model (Nov-Jan), and is only slightly underestimated relative to the CZCS. Although large concentrations of chlorophyll are observed from *in situ* records during the southwest monsoon (Conkright et al., 1998d), there is reason to suspect the magnitudes that the CZCS observes (which exceed 3 mg m^{-3} over large parts of the Arabian Sea). The primary reason is that this is a region adversely impacted by absorbing aerosols originating from nearby desert regions. These absorbing aerosols are incorrectly identified in the CZCS processing, and thus will result in overestimates of pigment if they are present. However, Tindale and Pease (1999) found lower dust contributions to the total aerosol during the southwest monsoon.

Seasonal variability in the tropics is often smaller than the interannual signal, especially in the Pacific. The only significant season influence is the motion of Inter-Tropical Convergence Zone (ITCZ), which is related to the sub-solar position. The model chlorophyll results reflect this lack of seasonal variability. However, the overestimate of tropical Pacific by the model is one of the most consistent trends in the comparison with CZCS pigment. The model appears to represent the seasonal trends (or lack of) here but not the magnitudes. *In situ* chlorophyll data from the NODC/OCL archives suggest mean concentrations of between 0.1 and 0.2 mg m^{-3} (Conkright et al., 1998c), which is more in agreement with the model means (about 0.17 mg m^{-3}), and in contrast to the CZCS (which has a mean of about 0.07 - 0.08 mg m^{-3}). Thus the model performance may actually be representative.

In the Southern Hemisphere, seasonal distributions of chlorophyll from the model are once again generally in agreement with CZCS in both timing and magnitude (Figure 6). The South Indian, Pacific, and Atlantic Oceans indicate a seasonal maximum occurring in mid-to-late austral winter (June-to-August). The model agrees with this trend, except that the model predicts the elevated

biomasses are sustained longer than the CZCS appears to indicate. In the South Atlantic the maximum arises in the model about two months later than the CZCS. Magnitudes in all three regions computed by the model are in very good agreement with the CZCS. The biomass peaks arise in the model due to mixed layer deepening occurring in the austral winter, similar to the processes described earlier for the North Central Pacific and Atlantic. Again the injection of nutrients into the mixed layer deepening are insufficient to allow profuse phytoplankton growth due to the depth of the layer itself, producing low irradiance availability experienced by the phytoplankton.

The Antarctic region is a bloom-recede region similar to the northern Pacific and Atlantic, governed by the solar cycle and its influences on mixed layer depth and irradiance availability. The peak biomass in the model is achieved somewhat later than the North Pacific and Atlantic in the model, occurring about 1 month after the austral summer solstice. It sustains at this maximum for a full month, unlike the northern sub-polar regions. The CZCS pigment peak extends from December to March. The delay in the model results from surface heating and mixed layer shallowing, which does not develop fully until February. Mixed layer depths here are generally deeper than in the northern sub-polar regions, requiring more heating to shallow, according to the model. Like the northern sub-polar regions, the period of elevated pigment concentrations in the Antarctic region extends well into the austral autumn and winter, and does not resemble the model results. However, exceptionally poor sampling of this region by the CZCS during this period almost certainly produces a bias such that the more northern portions of the region, where higher pigment exists (and also in the model), are over-represented in the mean. Where there is sampling in the more southerly portions, the results suggest agreement of the model with the CZCS. Otherwise, the general features of the Antarctic seasonal cycle and the chlorophyll concentrations produced by the model are in very good with the CZCS.

Seasonal Trends in Chlorophyll: Synoptic Scale Comparisons with CZCS

Imagery of simulated chlorophyll provides a better view of the nature and spatial distributions of the seasonal variability and how it compares to CZCS pigment. Four months are chosen to represent some of the range of seasonal variability exhibited by the model and observed in the CZCS (Figures 7 and 8). Generally, large scale features are well-represented in the model and conform to CZCS data: vast areas of low chlorophyll in the mid-ocean gyres, elevated chlorophyll in the equatorial and coastal upwelling regions, and large concentrations in the sub-polar regions. The large scale features of the seasonal variability are represented as well: blooms of chlorophyll in local spring/summer in the high latitudes, followed by retreat in the local winter; expansion of low chlorophyll gyre regions in local summer, followed by contraction in winter; enhancement in the Indian Ocean in August and December, and reduced concentrations in March and May. These features are evidence of realism in the model and its ability to simulate synoptic scale patterns and variability.

March represents a transition period, when phytoplankton growth in the Southern Hemisphere is diminishing and growth in the Northern Hemisphere is accelerating (Figure 7). The beginning of the Northern Hemisphere spring bloom is apparent in both the model and the CZCS. The latitudinal extent is limited to about 50° N. In the model, this results from increasing day length and reduced solar zenith angles in the Northern Hemisphere, and some mixed layer shallowing. Remnants of the Southern Hemisphere bloom are still apparent in CZCS imagery, especially near New Zealand, the Scotian Sea, and the Patagonian shelf. The Patagonian shelf is well-represented by the model, but

the New Zealand area is underestimated, and the region of high chlorophyll in the Scotian Sea is displaced to the south. The model shows very low chlorophyll in proximity of the ice distribution, while the CZCS is somewhat higher, although variable. It is likely that large pigment concentrations in this region in the CZCS are artifacts due to the presence of ice. Low chlorophyll concentrations near the ice sheets in the model are due to very cold temperatures, limiting the maximum growth rate. Coupled with continued sinking throughout the austral winter, phytoplankton populations become too small to sustain themselves for the duration of the non-growth season. This is in spite of reduced grazing accompanying the low temperatures. Temperatures attain the model minimum of -2°C here during the austral winter. The model requires a formulation of ice algal dynamics, and austral spring melting and seeding in order to reasonably simulate this area. Such dynamics have been shown to be substantial contributors to the total primary production in these regions (Arrigo et al., 1997). Overall the spatial variability of pigment distributions in CZCS is much larger than model chlorophyll. The model is driven by winds, sea surface temperatures, and cloud cover, which are apparently insufficient to capture the spatial variability apparent in the CZCS. In the search for reasons for the discrepancy, it may be due to the lack of circulation or mixing variability that is unavailable in the reduced gravity representation of the circulation model, or that iron limitation is at work here (Martin et al., 1990), although mechanisms causing spatial variability are elusive.

The sub-polar transition zones in the South Atlantic, Indian, and Pacific Oceans are almost replicated in the model, although the model exhibits generally larger concentrations and less spatial variability. The North Central Pacific gyre is smaller in size in the model than in the CZCS, but the Southern Hemisphere mid-ocean gyres are almost matched. Deep mixed layers with strong density interfaces are prevalent in the model in these regions this time of year in the model, suppressing phytoplankton growth by lack of nutrients and low average irradiance availability.

The tropical Pacific upwelling region has about twice the chlorophyll concentration in the model as in CZCS pigment, but the meridional and zonal extent is nearly the same (Figure 7). This suggests either excessive upwelling in the model or the lack of iron as a limiting nutrient in the model. This region is widely regarded as iron limited (Kolber et al., 1994; Coale et al., 1998). Tropical Atlantic and Indian Ocean features in CZCS pigment are well represented in the model, although somewhat overestimated by the model in the Atlantic. Upwelling off the Mauritanian and Namibian coasts is represented in the model, although with reduced peak values. The model underestimates the chlorophyll concentrations in the Arabian Sea and North Indian Ocean, but many of the same features are apparent. March corresponds to the inter-monsoon season here, but the season has not reached its maximum yet. High chlorophyll offshore of Costa Rica is apparent in both. This is strictly a boundary-induced upwelling feature in the model, but in the CZCS may be additionally influenced by the Coast Rica dome. The California coast exhibits strong upwelling in both the model and imagery.

In May the Northern Hemisphere spring bloom is in full swing in CZCS imagery, and is very nearly matched in the model (Figure 7). The northerly extent of the bloom extends to the edge of the model domain in the CZCS imagery, and nearly so in the model. There is more spatial variability in the North Pacific in the CZCS than in the model, but magnitudes and extent are very similar. There are many specific features of the North Atlantic bloom that differ between model and CZCS, but the overall structure and magnitude is similar. The model results are the classic result of increased solar heating producing a shallow mixed layer replete with nutrients from the long boreal winter, longer

days and higher solar zenith angles to support phytoplankton growth, and lagging zooplankton populations producing low grazing. Temperatures remain somewhat low to keep the magnitude of the bloom down, helping to produce the agreement with the CZCS.

The North Pacific and Atlantic gyres exhibit expansion from March in both the model and CZCS. The shapes of the mid-ocean gyre regions do not conform, but because of only slightly larger values in the model at the periphery of the gyre in the Pacific (0.08-0.1 mg m⁻³ in the model compared to 0.04-0.08 mg m⁻³ in the CZCS). The North and equatorial Indian Oceans also have substantially reduced pigment concentrations. This is in good agreement with the model, which is the result of the inter-monsoon season being fully underway, with light winds, sluggish circulation patterns, and deeper mixed layers.

The Southern Hemisphere gyres, in contrast to the Northern ones, exhibit contraction in May compared to March. This is true for both the model and CZCS, and sizes/magnitudes are almost replicated in the model. The mixed layer is deepening in the model producing availability of nutrient from below. The Patagonian shelf and South Atlantic sub-polar transition zones are both diminished in chlorophyll relative to March, resulting in the model from higher solar zenith angles and shorter day length. Again these trends are represented in both the model and CZCS. The Australia/New Zealand region of high pigment in CZCS is reduced in magnitude and extent in May, as it also is in the model, but again the model appears to underestimate the magnitude. The reduced gravity approximation, lack of boundary effects originating from the nearby land (nutrient input) are possible explanations. Coverage south of -50° latitude is sparse in the CZCS, and the model is the only source of data. Where CZCS data exist, they appear to be in good agreement with the model, exhibiting a major advantage of numerical simulation.

In August the extent of the high latitude high pigment regions in the North Pacific and Atlantic is reduced as the gyres have expanded (Figure 8). Both model and CZCS show similar patterns. Magnitudes have fallen slightly in the model due to mild nutrient limitation, but appear to be sustained in the CZCS. The model now exhibits high chlorophyll to the northern edge of the domain, as does the CZCS. This is due to heat flux finally exerting influence in these northerly regions, coupled with nearly constant day and associated high solar zenith angles in the model. Very large expansion of the Northern Hemisphere mid-ocean gyres has occurred, in both model and CZCS. In the model this is due to reduction of mixed layer depths and nutrient exhaustion.

Large pigment biomasses are observed in the CZCS in the North Indian Ocean and Arabian Sea. As noted earlier, the August North Indian is the largest mean biomass observed by the CZCS in its entire history. The model also shows major increases in chlorophyll concentrations, due to the intensification of the southwest monsoon. But the model is not nearly as dramatic. The CZCS indicates a very large area of pigment values >1 and often >3 mg m⁻³ in the Arabian Sea. Gardner et al. (1999) reported maximum surface values of about 3 mg m⁻³ during the late southwest monsoon, which quickly dissipated to about 1.2 mg m⁻³ in two days. This represented a time series of three days. The dynamics are present to produce these high concentrations, but *in situ* data from the NODC/OCL archive for summer indicate mean chlorophyll values not exceeding 0.4-0.5 in this area (Conkright et al., 1998d) which is very much in agreement with the model.

Enhancement of CZCS pigment in the tropical Atlantic is very strong in August, as it also is in the model (Figure 8). The ITCZ is shifted northward and consequently reduced cloud cover overlies the region. Large pigment concentrations are apparent in the CZCS along the Namibian coast, which is

due to upwelling in the model. There is substantial contraction of the Southern Hemisphere gyres, along with some modest enhancement of the Patagonian shelf pigment. These patterns are nearly replicated by the model and are the result of mixed layer deepening and associated nutrient injection in the gyres and increased turbulent mixing in Patagonia. The observed portions of the Antarctic Ocean and sub-polar transition zones have larger mean pigment concentrations in the CZCS compared to May, as well as in the model. An exception is the diminished pigment near New Zealand, for which the opposite trend is found in the model. However, the net effect is to make the model chlorophyll in better agreement with the CZCS this month. The model predicts very low biomasses south of -50° latitude. This is the result of very cold temperatures ($< 0^{\circ}$ C) and nearly constant darkness. CZCS data are either obscured by clouds or unsampled, but the slivers that exist (e.g., near 180 W) suggest agreement with the model.

December pigment concentrations exhibit major reduction in magnitude in the northern sub-polar Pacific and Atlantic, along with contraction of the Northern Hemisphere mid-ocean gyres as the sub-polar regions of high pigment have moved south (Figure 8). These trends are well-represented by the model. There is intensification of pigment biomass in the CZCS along the western US coast that is not represented by the model. Again the model predicts larger chlorophyll concentrations in the tropical Pacific than the CZCS, but the extent is very well matched. Note especially the area of high chlorophyll north of the main axis of the tropical upwelling located between 160W and 100 W, which is also apparent in the CZCS. The tropical Atlantic shows intensification of pigment biomass in the CZCS from August, but the model shows a slight decrease in magnitude. High chlorophyll off the coast of Namibia has grown in the model from August, while it has diminished in the CZCS. The tropical and North Indian Ocean, and the Arabian Sea, are reduced in chlorophyll in both the model and CZCS from August, but are still much larger than in May. Southern Hemisphere gyres begin to exhibit expansion from their distribution in August, and the southern ocean is now increasing in chlorophyll and pigment. These trends are well represented by the model, but the CZCS shows much greater spatial variability than the model.

Seasonal Trends in Nitrate: Synoptic Scale Comparisons with *In situ* Data

Model surface nitrate results are averaged over seasons and compared to *in situ* archives maintained by NODC/OCL (Conkright et al., 1998b; 1998c; 1998d). The results show overall excellent agreement between model and data, and features of seasonal variability are in conformance (Figures 9 and 10). Spatial distributions and magnitudes are well represented by the model. Two general exceptions are the tropical Pacific and Atlantic. In both cases the model predicts much larger nitrate concentrations than are observed in the data. The departure is much reduced for summer and autumn in the Pacific, but the discrepancy in the Atlantic is persistent. *In situ* data show no apparent evidence of upwelling at all in the Atlantic, whereas the model exhibits strong upwelling. Given that the CZCS pigments clearly show high biomasses indicative of upwelling (Figures 7 and 8), and given the forces present, e.g., winds, coastal boundary, equatorial divergence, brings into question the *in situ* data here. Large pigment values as seen in the CZCS, especially in summer and autumn, cannot be sustained with the low nitrate values shown in the *in situ* data. However, there is the possibility the CZCS estimates are in error due to the presence of absorbing aerosols and/or colored dissolved organic matter in the water that produce a pigment-like signature.

Note how seasonal distributions of nitrate are represented in the North Pacific and Atlantic by the *in situ* data and the correspondence in model results (Figures 9 and 10). Large concentrations, with magnitudes and spatial extent matching the data, are apparent in winter, which diminish in spring. By summer magnitudes reach a minimum, and begin to recover by autumn. In the model, large nitrate concentrations in the winter are due to lack of utilization by phytoplankton, and availability through convective overturn in the boreal autumn and turbulent exchange. In boreal spring nitrate concentrations begin to diminish due to nutrient utilization by phytoplankton in spring, when conditions supporting acceleration of growth are available (shallowing mixed layer and irradiance availability). By summer the period of high phytoplankton growth has been occurring for several months, and little new exchange has occurred from deeper layers, resulting in severe reduction (but not depletion). The reduction of nitrate in the North Atlantic is much greater than in the Pacific. CZCS pigments suggest much larger biomasses in the N. Atlantic than Pacific, which would result in reduced nitrate concentrations in the Atlantic. The model, however, shows greater chlorophyll concentrations in the Pacific, which are due to the large availability of nitrate at the beginning of the growing season. Given that the nitrate concentrations appear to be correct in the model, this suggests that phytoplankton are limited in the North Pacific by some process or substance that is not explicit in the model. Again iron limitation is a possibility (Martin and Fitzwater, 1988). But more perplexing is the presence of large CZCS pigments in summer in the Atlantic associated with relatively low nitrate. By autumn nitrate concentrations are beginning to be replenished as phytoplankton growth decreases from mixed layer deepening and reduced irradiance.

The Arabian Sea exhibits moderate nitrate values in winter, diminishing in spring, and attaining the maximum in summer. These trends are well represented by the model, and are the direct result of circulation patterns associated with the southwest and northeast monsoons, and the inter-monsoon periods.

Phytoplankton Group Distributions

Phytoplankton group distributions are initialized as equal values across the model domain (Figure 11). In April after 4 years of simulation, the three phytoplankton functional groups arrive at distributions that generally conform to expectations: diatoms dominate high latitude, coastal, and equatorial upwelling regions, picoplankton dominate the central ocean gyres, and chlorophytes inhabit transitional regions (Figure 12). These distributions are not monthly means but represent a single day at the beginning of the month. The diversity of the functional groups, and their different abilities to survive under different oceanic habitats, is the main reason for the overall success of the model in representing global chlorophyll patterns. Diatoms bloom first in the North Atlantic and the eastern North Pacific, and dominate the Antarctic Ocean and sub-polar transition region. Eynaud et al. (1999) also found that diatoms were predominant in the Antarctic Ocean but also found that coccolithophores predominated in the Antarctic sub-polar transition region. Chlorophytes dominate the western North Pacific and the edges of the equatorial upwelling regions outside the area dominated by diatoms. They also predominate at the edge of the sub-polar transition region in the south, and have very large populations in the southern ocean from about 40°W eastward to 70°E. Picoplankton are generally distributed throughout the central gyres at low concentrations, but have some larger abundances in the western North Pacific and Atlantic at the edge of the diatom blooms, in the southern periphery of the tropical Pacific upwelling, and offshore of Namibia. The

predominance of picoplankton in the mid-ocean gyres is well established (Glover, 1985; Ituriaga and Mitchell, 1986; Ituriaga and Marra, 1988).

In the model, diatoms follow the nutrients. Where there are abundant nutrient concentrations, diatoms tend to be prevalent. These regions occur in the model where kinetic energy is large: where convective overturn results in massive displacement of vertical water masses, where turbulent mixing processes are large, and upwelling circulation is vigorous. These are the high latitudes, coastal upwelling areas, equatorial upwelling areas, and regions of strong seasonal influences such as the Arabian Sea. This is because diatoms are the fastest growing of the functional groups contained in the model. This enables them to outcompete the other groups when nutrients and light are available. However, their large sinking rates prevent them from sustaining their populations in quiescent regions or periods. Thus they require light and nutrients to produce growth rates that can enable them to sustain the large losses they incur from their sinking rates. These areas occur in the high kinetic energy regions of the global oceans.

Picoplankton are nearly the functional opposite of diatoms in the model. Slow growing and nearly neutrally buoyant, they cannot compete with diatoms under favorable growth conditions, but have a competitive advantage in low nutrient, by virtue of the low sinking rates and to a very minor extent their ability to fix molecular nitrogen. Thus they dominate in quiescent regions, such as mid-ocean gyres, where kinetic energy is low, circulation is sluggish, mixed layer depths are deep, and nutrients are only occasionally injected into the mixed layer. While they are able to survive in these regions, the lack of nutrients and deep mixed layers produce an overall low average irradiance environment and they never attain large concentrations. They occasionally attain some moderate concentrations, e.g., 0.25 mg m^{-3} , in isolated regions of the oceans. Some examples are the southern portion of the high chlorophyll regions in the north Pacific and Atlantic, the periphery of the tropical Pacific upwelling, and the periphery of the Benguela upwelling. Each case represents a transition zone from a high chlorophyll diatom-dominated region.

Chlorophytes generally represent a transitional group in the model, inhabiting areas where nutrient and light availability are insufficient to allow diatoms to predominate, but not in areas where nutrients are so low to prevent losses by sinking to compensate by growth. This is a function of their intermediate growth and sinking rates relative to diatoms and picoplankton. Their largest concentrations tend to be at the transition between the diatoms and picoplankton, such as the southern edge of the northern spring bloom (vice versa for the southern bloom), or the edges of the tropical upwelling and Arabian Sea blooms. They are most responsible for the seasonal expansion/contraction of the mid-ocean gyres, which is one of the most significant seasonal signals in the model and in the CZCS record.

The North Pacific represents somewhat of an anomaly in chlorophyte distribution, since they tend to dominate the western portion where one would expect diatoms to prevail. This part of the Pacific is exceptionally cold and the success of chlorophytes here is due to their overwintering advantage provided by their lower sinking rates. The cold temperatures suppress maximum growth rates of all groups, but the difference between diatoms and chlorophytes is less in cold water, allowing their lower sinking rates to provide a competitive advantage.

Similar overall distributions of the phytoplankton groups are observed in October as in April, except some facets are reversed in hemisphere (Figure 13). Chlorophytes comprise a larger proportion of the total chlorophyll in the North Pacific and Atlantic. The remnants of the southwest

monsoon in the Arabian Sea can be seen and is dominated by diatoms. The southern ocean is beginning the austral spring bloom and is predominantly diatoms, with chlorophytes at the periphery. Picoplankton are again widely distributed and in low abundances, but with some local blooms, such as the edge of the high chlorophyll transition zone in the southern Atlantic.

Diatom dominance of the equatorial Pacific is counter to observations in the region (e.g. Cahvez, 1989; Landry et al., 1997; Brown et al., 1999), which indicate a pico-nano-plankton dominated community. The prevalence of nutrients and low chlorophyll, along with associated low biomasses of diatoms in conditions that should support large populations and their associated blooms, is one of the driving influences behind the iron limitation hypothesis. Diatoms appear to be especially subject to iron availability (Miller et al., 1991; Morel et al., 1991a; b; Price et al., 1994). However, diatom abundance is found to be larger very near the axis of the Pacific upwelling region (Landry et al., 1997), where iron availability is higher than outside of this band. Since this model does not contain explicit iron regulation, predominance by picoplankton cannot be reproduced. Thus the model produces phytoplankton group population structure that is reasonable in the absence of iron limitation, and clearly such effects need to be incorporated in future enhancements.

Seasonal variability of the phytoplankton groups is shown for four regions that are representative of most of the range of the global oceans. The four regions are the North Atlantic (sub-polar region with pronounced spring bloom regions and fall/winter die-off), North Central Pacific (a low chlorophyll biomass central gyre), North Indian Ocean (monsoon-dominated region), and the equatorial Atlantic (representing a tropical upwelling region).

The North Atlantic exhibits a classic pattern of seasonal succession, with diatoms dominating early in the year as the mixed layer begins to shallow and light begins to become available, giving way to dominance by chlorophytes in late summer as the mixed layer stabilizes at shallow depth and nutrients become limiting, and lasting under autumn when fall overturn injects nutrients into the mixed layer and favors diatoms again. Picoplankton provide a low and steady proportion of the total population, but increase slightly in the dead of boreal winter due to reduced losses from sinking and depletion when conditions for growth of diatoms improves.

The North Central Pacific exhibits a similar seasonal succession pattern, except that it is between diatoms and picoplankton. The group changeover also occurs earlier in the boreal summer than the North Atlantic. Diatoms are prevalent in winter when mixed layer deepening entrains nutrients, fostering growth. Later in the year, when the mixed layer shallows and nutrients are exhausted, the picoplankton predominate. Chlorophytes in the North Central Pacific maintain low and seasonally invariant populations, but are actually changing position latitudinally in response to the enhancement and contraction of the mid-ocean gyre.

The North Indian Ocean is subject to four major seasonal influences, the southwest monsoon peaking in August, the less vigorous northeast monsoon occurring through the boreal winter, and 2 inter-monsoon periods between them. The abundances of diatoms follow the pattern of the monsoons, while picoplankton and chlorophytes respond more favorably to the inter-monsoon seasons. This generally conforms to observations in the region (Brown et al., 1999). In the model, this is due to the presence of nutrients resulting from turbulence and upwelling associated with the monsoon periods, and favoring diatom growth. The extent of the diatom dominance is directly related to the strength of the monsoon period: they comprise >80% in the more vigorous southwest monsoon compared to slightly < 50% in the less vigorous northeast monsoon. Losses of diatoms

from sinking in the inter-monsoon periods allow chlorophytes and picoplankton to outcompete the diatoms for the low concentrations of nutrients.

The equatorial Atlantic exhibits a very different seasonal pattern than the other regions. In this region, chlorophytes dominate the total chlorophyll throughout the year, yielding to diatoms for only a small period centered about the boreal solstice. These patterns follow the periods of upwelling in the Atlantic (Monger et al., 1997). Picoplankton exhibit very little seasonal variability.

Summary and Conclusions

Global computed chlorophyll and nitrate from a coupled ocean general circulation, biological, and radiative model compare very well with satellite and *in situ* sources. Generally, large scale chlorophyll features such as the location, size, and shape of mid-ocean gyres, equatorial upwelling regions, high latitudes, and coastal upwelling regions are in very good agreement with CZCS pigments. Moreover, the seasonal dynamics agree favorably as well. Shifts of high chlorophyll across hemispheres are in correspondence, as are timing features of bloom-and-recede. The mid-ocean gyres expand in the local summer and contract in local winter in accordance with mixed layer shallowing and deepening, respectively, and match cycles indicated in the CZCS. Basin scale seasonal trends are in agreement with those determined from the CZCS in every oceanic basin.

Seasonal comparisons with *in situ* nitrate climatologies exhibit even better correspondence. The location, seasonal dynamics, and magnitudes are almost matched by the model. A prominent exception is the equatorial Atlantic upwelling region, which appears prominently in the model but is not indicated in the data. Considering that CZCS pigment concentrations clearly suggest upwelling, and that the agreement with the model elsewhere suggests problems with the data set.

The agreement of the model with satellite and *in situ* data is nearly always good, and at times remarkable. Considering that the model is initialized with flat fields of chlorophyll, this suggests realism in the physical, biological, and radiative dynamics included in the model, at least at synoptic scales. At times of poor sampling by the CZCS, such as local winter at the high latitudes, the model appears to produce better estimates of chlorophyll concentrations, since the CZCS only sampled the portions toward lower latitudes which always had higher estimates. This leads to an overestimate of mean pigment in these seasons, while the model results are unbiased, and incidentally, generally in agreement where small pockets of CZCS sampling occurred.

The model contains 3 phytoplankton groups whose distributions are initialized as equal amounts throughout the model domain. After four years of simulation, they arrive at reasonable distributions throughout the global oceans: diatoms dominate high latitudes, coastal, and equatorial upwelling areas, picoplankton dominate the mid-ocean gyres, and chlorophytes represent a transitional assemblage, occurring predominantly in regions unoccupied by the others. Diatoms are responsible for high chlorophyll regions, while chlorophytes are mostly responsible for seasonal changes in the mid-ocean gyres, i.e., contraction in local winter and expansion in local summer. Seasonal patterns exhibit a range of relative responses: from a classic seasonal succession in the high latitudes with chlorophytes replacing diatoms as the dominant group in mid-summer, to successional patterns with picoplankton replacing diatoms in mid-summer in the North Central Pacific. Diatoms are associated with high kinetic energy regions where nutrient availability is high. Picoplankton predominate in quiescent regions with low nutrients. These results are a direct response to differences in phytoplankton group maximum growth and sinking properties. The net effect of the phytoplankton

groups is the ability of the model to more accurately represent a wider range of oceanic habitats simultaneously than is possible with a single group. Given that the global ocean is a diverse physically, biologically, and chemically, multiple groups are required to simulation accuracy and to represent the major features of seasonal variability.

Acknowledgements. This paper was not possible without the development of the Poseidon GCM by Paul Schopf, George Mason University Center for Ocean-Land-Atmospheres, and the provision of code for integration. Michele Rienecker, NASA/GSFC, provided meaningful insight into the GCM results and dynamics. The NASA/Goddard Space Flight Center provided the CZCS data that was used for comparison. Margarita E. Conkright (NODC/OCL) provided *in situ* nitrate seasonal climatologies. This work was supported under NASA Grant (RTOP) 971-622-51-31.

References

- Ahn, Y.-H., A. Bricaud, and A. Morel, Light backscattering efficiency and related properties of some phytoplankters, *Deep-Sea Res.*, 39, 1835-1855, 1992.
- Arrigo, K.R., D.L. Worthen, M.P. Lizotte, P. Dixon, and G. Dieckmann, Primary production in Antarctic sea ice, *Science*, 276, 394-397, 1997.
- Barlow, R.G. and R.S. Alberte, Photosynthetic characteristics of phycoerythrin-containing marine *Synechococcus* spp., *Mar. Bio.*, 86, 63-74, 1985.
- Bates, S.S. and T. Platt, Fluorescence induction as a measure of photosynthetic capacity in marine phytoplankton: response of *Thalassiosira pseudonana* (Bacillariophyceae) and *Dunaliella teriolecta* (Chlorophyceae), *Mar. Ecol. Prog. Ser.*, 18, 67-77, 1984.
- Ben-Amotz, A. and A. Gilboa, Cryptopreservation of marine unicellular algae. I. A survey of algae with regard to size, culture age, photosynthetic activity and chlorophyll - to - cell ratio. *Mar. Ecol. Prog. Ser.*, 2, 157-161, 1980.
- Bissett, W.P., J.J. Walsh, D.A. Dieterle, and K.L. Carder, Carbon cycling in the upper waters of the Sargasso Sea: I. Numerical simulation of differential carbon and nitrogen fluxes, *Deep-Sea Res.*, 46, 205-269, 1999.
- Brand, L.E., W.G. Sunda, and R.R.L. Guillard, Reduction of marine phytoplankton reproduction rates by copper and cadmium, *J. Exp. Mar. Biol. Ecol.*, 96, 225-250, 1986.
- Brand, L.E., W.G. Sunda, and R.R.L. Guillard, Limitation of marine phytoplankton reproductive rates by zinc, manganese, and iron, *Limnol. Oceanogr.*, 28, 1182-1198, 1983.
- Bricaud, A. and A. Morel, Light attenuation and scattering by phytoplanktonic cells: a theoretical modeling, *Appl. Opt.*, 25, 571-580, 1986.
- Bricaud, A., A. Morel, and L. Prieur, Optical efficiency factors of some phytoplankters. *Limnol. Oceanogr.*, 28, 816-832, 1983.
- Bricaud, A., A.-L. Bedhomme, and A. Morel, Optical properties of diverse phytoplanktonic species: experimental results and theoretical interpretation, *J. Plank. Res.*, 10: 851-873, 1988.
- Brown, S.L., M.R. Landry, R.T. Barber, L. Campbell, D.L. Garrison, and M.M. Gowing, Picophytoplankton dynamics and production in the Arabian Sea during the 1995 southwest monsoon, *Deep-Sea Res.*, 46, 1745-1768, 1999.
- Carpenter, E.J. and K. Romans, Major role of the cyanobacterium *Trichodesmium* in nutrient

- cycling in the North Atlantic Ocean, *Science*, 254, 1356-1358, 1991.
- Chavez, F.P., Size distribution of phytoplankton in the central and eastern tropical Pacific, *Global Biogeochemical Cycles*, 3, 27-35, 1989.
- Coale, K.H., K.S. Johnson, S.E. Fitzwater, S.O.G. Blain, T.P. Stanton, and T.L. Coley, Iron Ex-I, and *in situ* iron-enrichment experiment: Experimental design, implementation, and results, *Deep-Sea Res.*, 45, 919-945, 1998.
- Conkright, M.E., S. Levitus, T.O'Brien, T.P. Boyer, C. Stephens, D. Johnson, L. Stathoplos, O. Baranova, J. Antonov, R. Gelfeld, J. Burney, J. Rochester, and C. Forgy, *World Ocean Database 1998 CD-ROM Data Set Documentation*, National Oceanographic Data Center, Silver Spring, MD, 1998a.
- Conkright, M.E., T.O'Brien, S. Levitus, T.P. Boyer, C. Stephens, J. Antonov, *World ocean atlas 1998 Volume 10. Nutrients and chlorophyll of the Atlantic Ocean*, NOAA Atlas NESDIS 36, 217pp., 1998b.
- Conkright, M.E., T.O'Brien, S. Levitus, T.P. Boyer, C. Stephens, J. Antonov, *World ocean atlas 1998 Volume 11. Nutrients and chlorophyll of the Pacific Ocean*. NOAA Atlas NESDIS 37, 217pp., 1998c.
- Conkright, M.E., T.O'Brien, S. Levitus, T.P. Boyer, C. Stephens, J. Antonov, *World ocean atlas 1998 Volume 12. Nutrients and chlorophyll of the Indian Ocean*. NOAA Atlas NESDIS 38, 217pp., 1998d.
- Conkright, M.E., S. Levitus and T.P. Boyer, *World Ocean Atlas, Volume 1: Nutrients*, NOAA Atlas NESDIS 1, 150 pp., 1994a.
- Conkright, M.E., S. Levitus and T.P. Boyer, *Quality Control of Historical Nutrient Data*, NOAA Technical Memorandum 79, 75 pp., 1994b.
- Csanady, G.T., Mass transfer to and from small particles in the sea, *Limnol. Oceanogr.*, 31, 237-248, 1986.
- Da Silva, A.M., C.C. Young, and S. Levitus, *Atlas of surface marine data 1994 Volume 1: Algorithms and procedures*, NOAA Atlas NESDIS 6, 83 pp., 1994.
- Dubinsky, Z. and T. Berman, Light utilization efficiencies of phytoplankton in Lake Kinneret (Sea of Galilee), *Limnol. Oceanogr.*, 21, 226-230, 1986.
- Dugdale, R.C. and J.J. Goering, Uptake of new and regenerated forms of nitrogen in primary productivity, *Limnol. Oceanogr.*, 12, 196-206, 1967.
- Eppley, R.W., Temperature and phytoplankton growth in the sea, *Fish. Bull.*, 70, 1063-1085, 1972.
- Eppley, R.W., J.N. Rogers, and J.J. McCarthy, Half-saturation constants for uptake of nitrate and ammonium by marine phytoplankton, *Limnol. Oceanogr.*, 14, 912-920, 1969
- Eppley, R.W. and B.J. Peterson, Particulate organic matter flux and planktonic new production in the deep ocean, *Nature*, 282, 677-680, 1979.
- Eynaud, F., J. Girardeau, J.-J. Pichon, and C.J. Pudsey, Sea-surface distribution of coccolithophores, diatoms, silicoflagellates, and dinoflagellates in the South Atlantic Ocean during the late austral summer 1995, *Deep-Sea Res.*, 46, 451-482, 1999.
- Furnas, M.J., Net *in situ* growth rates of phytoplankton in an oligotrophic, tropical shelf ecosystem, *Limnol. Oceanogr.*, 36, 13-29, 1991.
- Gardner, W.D., J.S. Gundersen, M.J. Richardson, and I.D. Walsh. The role of seasonal and diel

- changes in mixed-layer depth on carbon and chlorophyll distributions in the Arabian Sea. *Deep-Sea Res.* 46: 1833-1858, 1999.
- Gavis, J., R.R.L. Guillard, and B.L. Woodward, Cupric ion activity and the growth of phytoplankton clones isolated from different marine environments, *J. Mar. Res.*, 39, 315-333, 1981.
- Glover, H.E., The physiology and ecology of the marine cyanobacterial genus *Synechococcus*, *Adv. Microbiol.*, 3, 49-107, 1985.
- Gregg, W.W. and K.L. Carder, A simple spectral solar irradiance model for cloudless maritime atmospheres, *Limnol. Oceanogr.*, 35, 1657-1675, 1990.
- Gregg, W.W. and J.J. Walsh, Simulation of the 1979 spring bloom in the Mid-Atlantic Bight: A coupled physical/ biological/optical model, *J. Geophys. Res.*, 97, 5723-5743, 1992.
- Gregg, W.W., Radiative impacts of clouds on phytoplankton growth, *Global Change Biol.*, submitted, 1999.
- Humphrey, G.F., Photosynthetic characteristics of algae grown under constant illumination and light-dark regimes, *J. Exp. Mar. Biol. Ecol.*, 40, 63-70, 1979.
- Itturiaga, R. and B.G. Mitchell, Chroococcoid cyanobacteria: a significant component in the food web dynamics of the open ocean, *Mar. Ecol. Prog. Ser.*, 28, 291-297, 1986.
- Itturiaga, R. and J. Marra, Temporal and spatial variability of chroocoid cyanobacteria *Synechococcus* spp. specific growth rates and their contribution to primary productivity in the Sargasso Sea, *Mar. Ecol. Prog. Ser.*, 44, 175-181, 1988.
- Kiefer, D.A. and B.G. Mitchell, A simple, steady state description of phytoplankton growth based on absorption cross section and quantum efficiency, *Limnol. Oceanogr.*, 28, 770-775, 1983.
- Kirk, J.T.O., Spectral properties of natural waters: Contribution of the soluble and particulate fractions to light absorption in some inland waters of southeastern Australia, *Australian Journal of Marine and Freshwater Research*, 31, 287-296, 1980.
- Kolber, Z.S., R.T. Barber, K.H. Coale, S.E. Fitzwater, R.M. Greene, K.S. Johnson, S. Lindley, and P.G. Falkowski, Iron limitation of phytoplankton photosynthesis in the equatorial Pacific Ocean, *Nature*, 371, 145-148, 1994.
- Landry, M.R., R.T. Barber, R.R. Bidigare, F. Cahi, K.H. Coale, H.G. Dam, M.R. Lewis, S.T. Lindley, J.J. McCarthy, M.R. Roman, D.K. Stoecker, P.G. Verity, and J.R. White, Iron and grazing constraints on primary production in the central equatorial Pacific: An EqPac synthesis. *Limnol. Oceanogr.*, 42, 405-418, 1997.
- Langdon, C., On the causes of interspecific differences in the growth-irradiance relationship for phytoplankton. Part I. A comparative study of the growth-irradiance relationship of three marine phytoplankton species: *Skeletonema costatum*, *Olisthodiscus luteus*, and *Gonyaulax tamarensis*, *J. Plank. Res.*, 9, 459-482, 1987.
- Levitus, S. and T.P. Boyer, World ocean atlas 1994, Volume 4: temperature. NOAA Atlas NESDIS 4, US Dept. of Commerce, Washington, DC, 117 pp., 1994.
- Levitus, S., R. Burgett, and T.P. Boyer, World ocean atlas 1994, Volume 3: salinity. NOAA Atlas NESDIS 3, US Dept. of Commerce, Washington, DC, 93 pp., 1994.
- Longhurst, A., Seasonal cycles of pelagic production and consumption, *Prog. Oceanogr.*, 35, 77-167, 1995.
- Martin, J.H. and S.E. Fitzwater, Iron deficiency limits phytoplankton growth in the north-east Pacific subarctic, *Nature*, 331, 341-343, 1988.

- Martin, J.H., R.M. Gordon, and S.E. Fitzwater, Iron in Antarctic waters, *Nature*, 345, 156-158, 1990.
- McGillicuddy, D.J., J.J. McCarthy, and A.R. Robinson, Coupled physical and biological modeling of the spring bloom in the North Atlantic (I): Model formulation and one dimensional bloom processes, *Deep-Sea Res.*, 42, 1313-1357, 1995.
- Miller, C.B. and others, Ecological dynamics in the subarctic Pacific, a possibly iron-limited system, *Limnol. Oceanogr.*, 36, 1600-1615, 1991.
- Mitchell, B.G. and D.A. Kiefer, Chlorophyll a specific absorption and fluorescence excitation spectra for light-limited phytoplankton, *Deep-Sea Res.*, 35, 639-663, 1988.
- Monger, B., C. McClain, and R. Murtugudde, Seasonal phytoplankton dynamics in the eastern tropical Atlantic, *J. Geophys. Res.*, 102, 12389-12411, 1997.
- Morel, A., Chlorophyll-specific scattering coefficient of phytoplankton. A simplified theoretical approach, *Deep-Sea Res.*, 34, 1093-1105, 1987.
- Morel, A. and A. Bricaud, Theoretical results concerning light absorption in a discrete medium, and application to specific absorption of phytoplankton, *Deep-Sea Res.*, 28, 1375-1393, 1981.
- Morel, F.M.M., R.J.M. Hudson, and N.M. Price, Limitation of productivity by trace metals in the sea, *Limnol. Oceanogr.*, 36, 1742-1755, 1991a.
- Morel, F.M.M., J.G. Rueter, and N.M. Price, Iron nutrition of phytoplankton and its possible importance in the ecology of open ocean regions with high nutrient and low biomass, *Oceanography*, 4, 56-61, 1991b.
- Pacanowski, R.C. and G. Philander, Parameterization of vertical mixing in numerical models of the tropical ocean, *J. Phys. Oceanogr.*, 11, 1442-1451, 1981.
- Perry, M.J., M.C. Talbot, and R.S. Alberte, Photoadaptation in marine phytoplankton: response of the photosynthetic unit, *Mar. Biol.*, 62, 91-101, 1981.
- Platt, T., C. Caverhill, and S. Sathyendranath, Basin-scale estimates of oceanic primary production by remote sensing: The North Atlantic, *J. Geophys. Res.*, 96, 15147-15159, 1991.
- Pribble, J.R., J.J. Walsh, D.A. Dieterle, and F.E. Muller-Karger, Numerical analysis of shipboard and coastal zone color scanner time series of new production within Gulf Stream cyclonic eddies in the South Atlantic Bight, *J. Geophys. Res.*, 99, 7513-7538, 1994.
- Price, N.M., B.A. Ahner, and F.M.M. Morel, The equatorial Pacific Ocean: Grazer-controlled phytoplankton populations in an iron-limited ecosystem, *Limnol. Oceanogr.*, 39, 520-534, 1994.
- Roache, P.J., *Computational Fluid Dynamics*, Hermosa Publ., Albuquerque, NM., 446 pp., 1982.
- Sakshaug, E. and K. Andresen, Effect of light regime upon growth rate and chemical composition of a clone of *Skeletonema costatum* from the Trondheimsfjord, Norway, *J. Plank. Res.*, 8, 619-637, 1986.
- Sathyendranath, S., L. Lazzara, and L. Prieur, Variations in the spectral values of specific absorption of phytoplankton. *Limnol. Oceanogr.*, 32, 403-415, 1987.
- Sathyendranath, S., A. Longhurst, C.M. Caverhill, and T. Platt, Regionally and seasonally differentiated primary production in the North Atlantic, *Deep-Sea Res.*, 42, 1773-1802, 1995.
- Schopf, P.S. and A. Lough, A reduced gravity isopycnal ocean model: Hindcasts of El Nino, *Mon. Wea. Rev.*, 123, 2839-2863, 1995.

- Subba Rao, D.V., Growth response of marine phytoplankton to selected concentrations of trace metals, *Botanica marina*, 24, 369-379, 1981.
- Tindale, N.W. and P.P. Pease, Aerosols over the Arabian Sea: Atmospheric transport pathways and concentrations of dust and sea salt, *Deep-Sea Res.*, 46, 1577-1595, 1999.
- Walsh, J.J., D.A. Dieterle, F.E. Muller-Karger, R. Bohrer, W.P. Bissett, R.J. Varela, R. Aparicio, R. Diaz, R. Thunell, G.T. Taylor, M.I. Scranton, K.A. Fanning, and E.T. Peltzer, Simulation of carbon-nitrogen cycling during spring upwelling in the Cariaco Basin, *J. Geophys. Res.*, 104, 7807-7825, 1999.
- Wyman, M. and P. Fay, Underwater light climate and the growth and pigmentation of planktonic blue-green algae (Cyanobacteria) I. The influence of light quantity, *Proc. R. Soc. Lond.* 227, 367-380, 1986.

Table 1. Notation for governing equations and general parameters. Values are provided for the parameters and ranges are provided for the variables.

Symbol	Meaning	Value	Units
A	Diffusivity	Variable	$m^2 s^{-1}$
∇	Gradient operator	none	none
\mathbf{V}	Vector velocity	Variable	$m s^{-1}$
\mathbf{w}_s	Vector sinking rate of phytoplankton	0.0035-1.2	$m d^{-1}$
μ	Specific growth rate of phytoplankton	0-2	d^{-1}
g	Grazing rate by herbivores	0-2.15	d^{-1}
s	Senescence	0.05	d^{-1}
b	Nutrient/chlorophyll ratio	25 - 80	$\mu M (\mu g^{-1} l^{-1})$
n_1, n_2	Heterotrophic loss rates	0.1, 0.5	d^{-1}
r	Remineralization rate	0-0.008	d^{-1}
ϵ	Nutrient regeneration by senescence	0.25	d^{-1}
γ	Herbivore grazing efficiency	0.25	d^{-1}
R_m	Maximum grazing rate at 20° C	1.0	d^{-1}
R	Maximum grazing rate	0.48-2.15	d^{-1}
Λ	Ivlev constant	1.0	$(\mu M)^{-1}$
K_N	Half-saturation constant (nitrogen)	1.0	
K_S	Half-saturation constant (silica)	0.2	

Figure Captions

Figure 1. Diagrammatic representation of the coupled circulation, biogeochemical, and radiative model of the global oceans. Monthly climatological wind and atmospheric optical properties are used to drive the surface forcing. The hydrodynamics are affected directly through the wind stress, and indirectly through the conversion of irradiance energy to heat in the radiative transfer model. The radiative model affects the biogeochemical model by determining the amount of total spectral irradiance available for growth of phytoplankton. Nutrient availability and herbivore ingestion also regulate phytoplankton populations locally. Outputs from the model are spectral upwelling radiance, primary production (which is an explicit calculation derived from the growth functions), chlorophyll abundances for each of the phytoplankton groups, and nutrients (nitrate, ammonium, and silicate).

Figure 2. Diagrammatic representation of the biogeochemical model. Three phytoplankton components (diatoms, chlorophytes and a generalized picoplankton group representing prokaryotic

plankton) interact with three nutrient components (nitrate, ammonium, and silicate), and contribute to detritus when ingested or upon death, which returns to the ammonium pool immediately and the nitrate pool later upon remineralization. Herbivores ingest phytoplankton groups non-preferentially, and contribute to the ammonium pool through excretion, and eventually the nitrate pool upon death and remineralization.

Figure 3. Phytoplankton group biological characteristics. Picoplankton characteristics are mostly from cyanobacteria, but are intended to be generally representative of pico-prokaryotes. Values are means of reported data. Top: Maximum growth rate (from Brand et al., 1986; 1983; Furnas, 1991; Gavis et al., 1981; Subba Rao, 1981; Humphrey, 1979; Ben-Amotz and Gilboa, 1980; Eppley et al., 1969; Goldman and Glibert, 1982). Middle: Maximum sinking rates (derived from Stokes Law and representative phytoplankton sizes from Morel 1987; Bricaud and Morel, 1986; Sathyendranath et al., 1987; Bricaud et al., 1983; Dubinsky and Berman, 1986; Kirk, 1975; Morel and Bricaud, 1981; Mitchell and Kiefer, 1988; Ahn et al., 1992; Bricaud et al., 1988). Bottom: Light saturation parameters, I_k . Low light is defined as $< 50 \mu$ moles photons, medium light is 50-200, and high light is > 200 (from Perry et al., 1981; Wyman and Fay, 1986; Langdon 1987; Sakshaug and Andresen, 1986; Bates and Platt, 1984; Barlow and Alberte, 1985). These figures illustrate the biological variety incorporated into the coupled model.

Figure 4. Comparison of model-generated mean chlorophyll (solid line) with climatological monthly mean CZCS pigment in the Northern Hemisphere. Error bars on the CZCS pigment represent one-fourth the CZCS standard deviation. Seasonal trends are in large agreement, although the magnitude of the spring bloom in the North Pacific appears to be overestimated by the model.

Figure 5. Comparison of model-generated mean chlorophyll (solid line) with climatological monthly mean CZCS pigment in the tropics. Error bars on the CZCS pigment represent one-fourth the CZCS standard deviation. Seasonal trends in all regions are well-represented by the model, but the magnitude of the southwest monsoon in the Arabian Sea appears to be vastly underestimated by the model.

Figure 6. Comparison of model-generated mean chlorophyll (solid line) with climatological monthly mean CZCS pigment in the Southern Hemisphere. Error bars on the CZCS pigment represent one-fourth the CZCS standard deviation. Seasonal trends in all regions are well-represented by the model, except perhaps the South Atlantic.

Figure 7. Computed chlorophyll distributions for March and May (monthly means) and CZCS mean monthly pigment for the same months for comparison. Climatological monthly ice distributions are indicated, but are not part of the model computations. General features of chlorophyll distributions are in agreement.

Figure 8. Computed chlorophyll distributions for August and December (monthly means) and CZCS mean monthly pigment for the same months for comparison. Climatological monthly ice distributions are indicated, but are not part of the model computations.

Figure 9. Comparison of model-computed surface nitrate distributions (averaged over seasons) with *in situ* data archives from NODC/OCL for winter and spring. Units are μM .

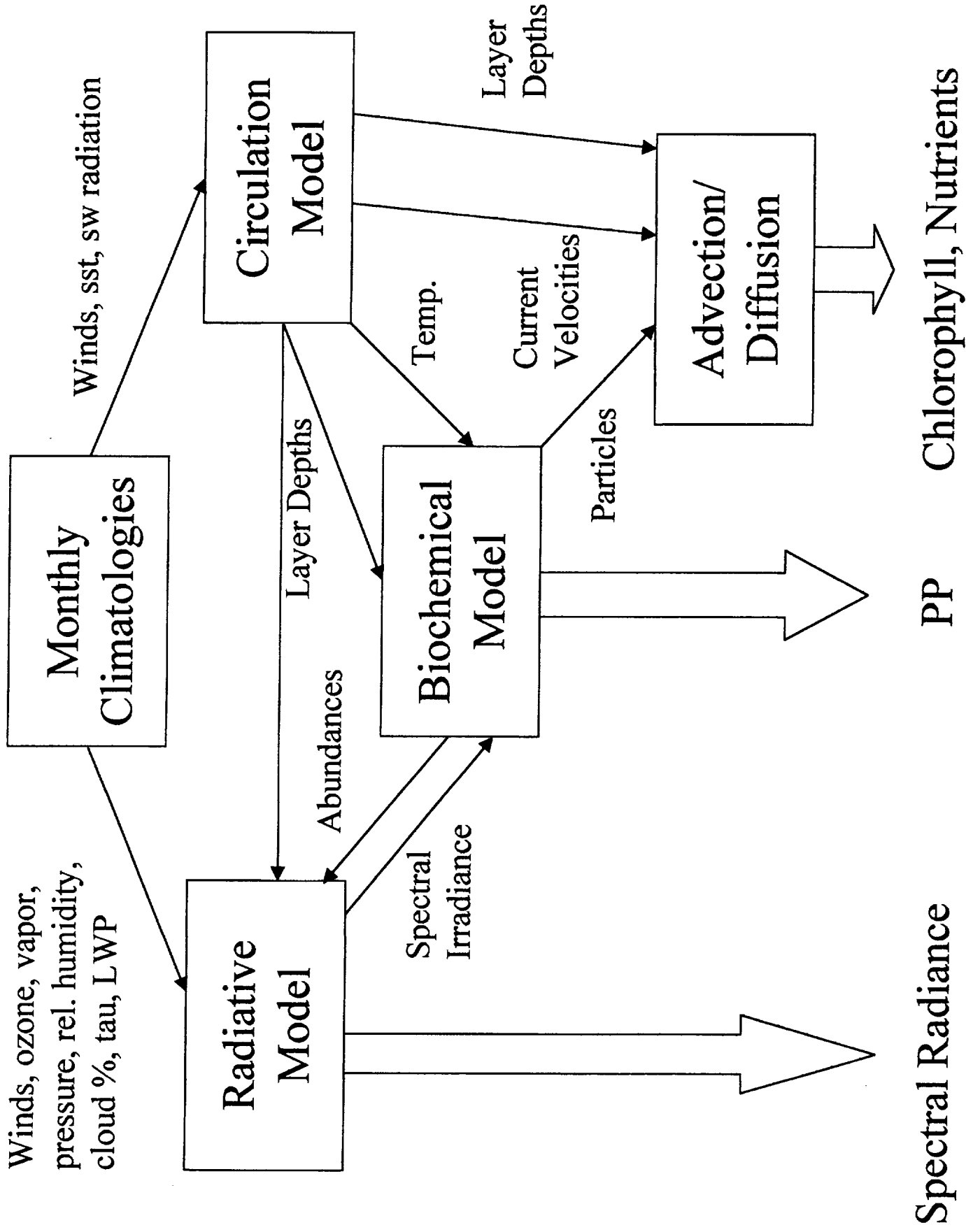
Figure 10. Comparison of model-computed surface nitrate distributions (averaged over seasons) with *in situ* data archives from NODC/OCL for summer and autumn. Units are μM .

Figure 11. Initial surface conditions for the 3 functional phytoplankton groups in the coupled model (mg m^{-3}). Depth distributions are the same.

Figure 12. Phytoplankton group distributions and total chlorophyll (sum of the three functional groups) computed for April after 4 years of simulation.

Figure 13. Phytoplankton group distributions and total chlorophyll (sum of the three functional groups) computed for October after 4 years of simulation.

Figure 14. Seasonal variability of phytoplankton groups in 4 regions, chosen to be representative of the range of most conditions in the global oceans. The groups are shown as proportion of the total in percent.



Winds, ozone, vapor, pressure, rel. humidity, cloud %, tau, LWP

Monthly Climatologies

Winds, sst, sw radiation

Radiative Model

Circulation Model

Biochemical Model

Advection/ Diffusion

Spectral Irradiance

Abundances

Layer Depths

Temp.

Current Velocities

Particles

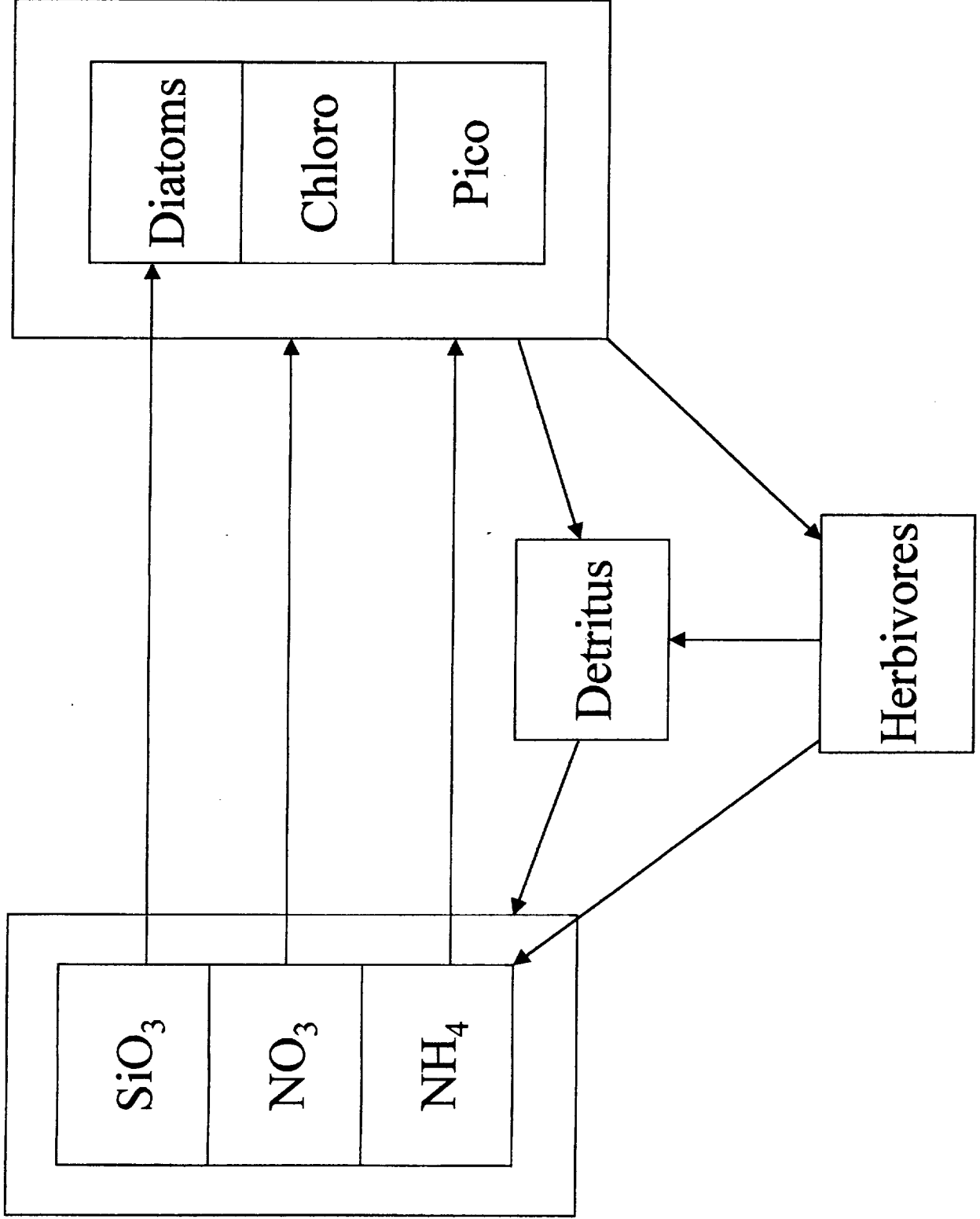
Layer Depths

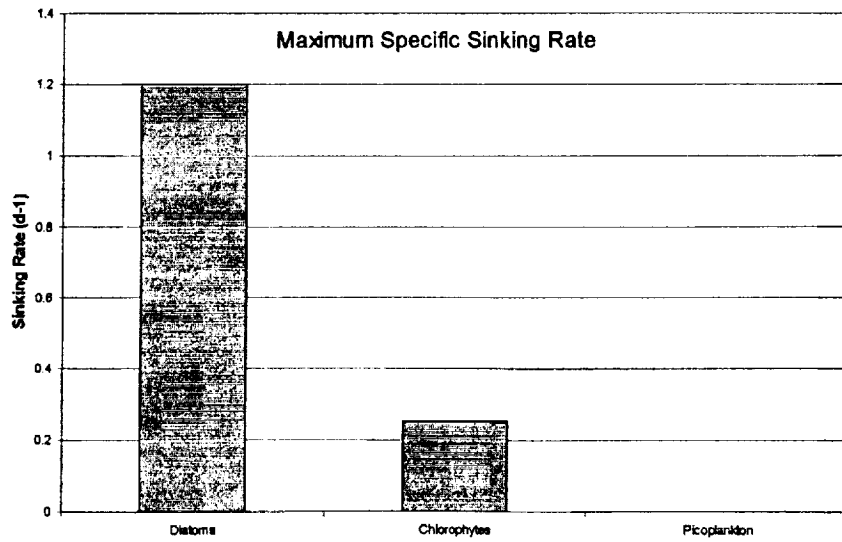
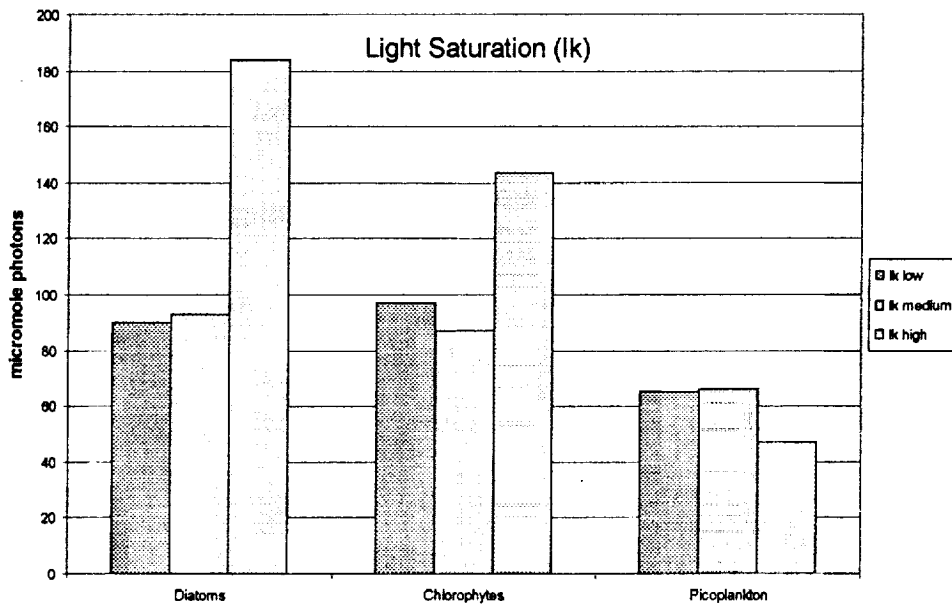
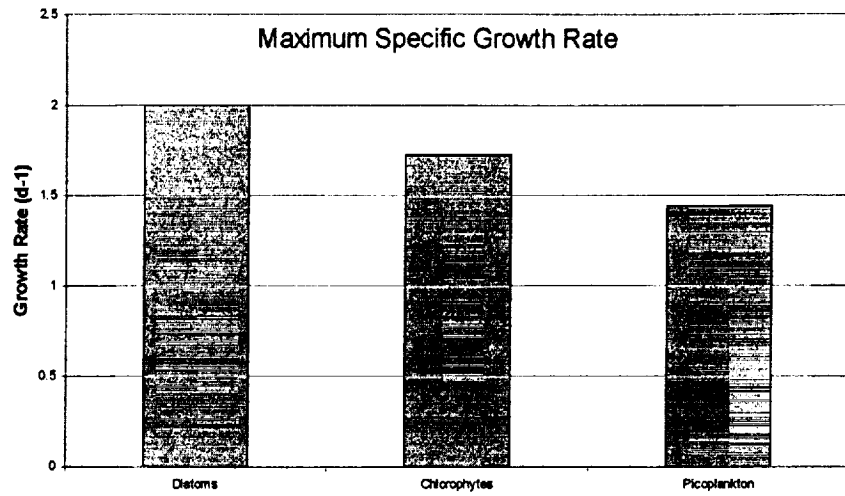
Spectral Radiance

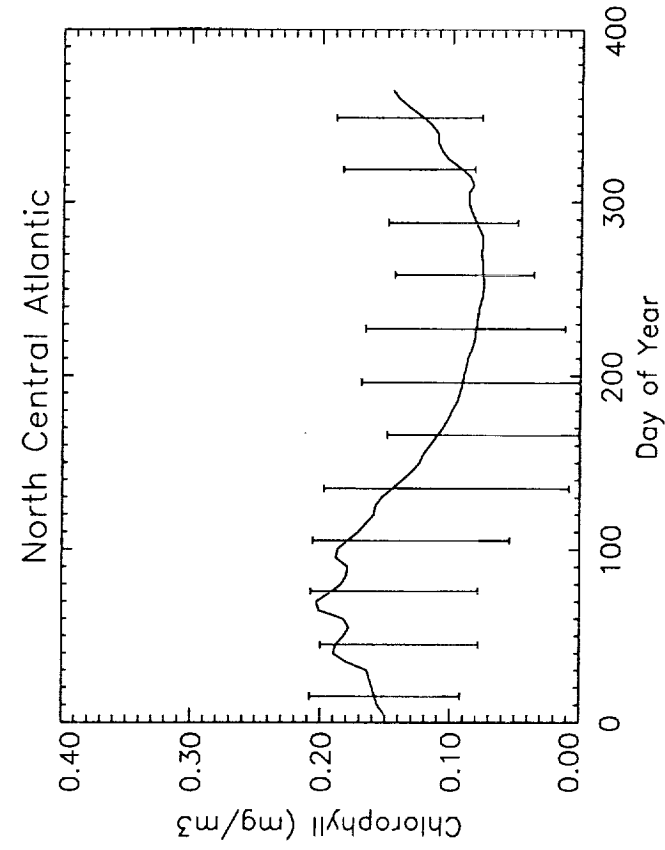
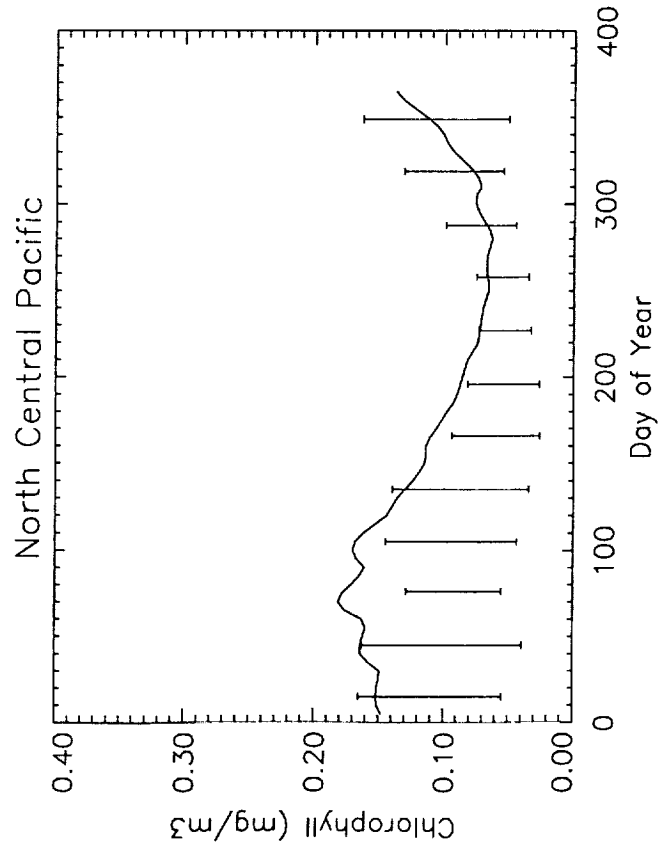
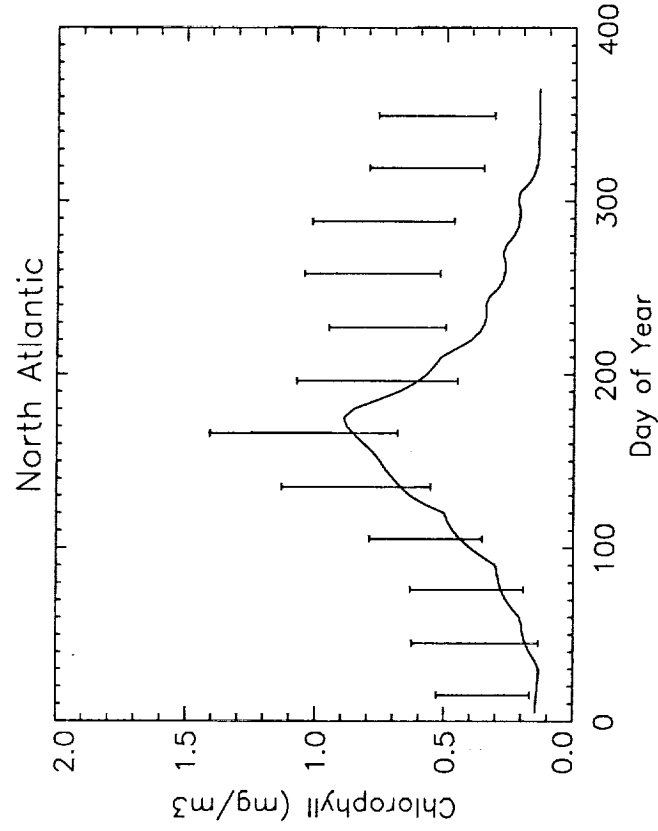
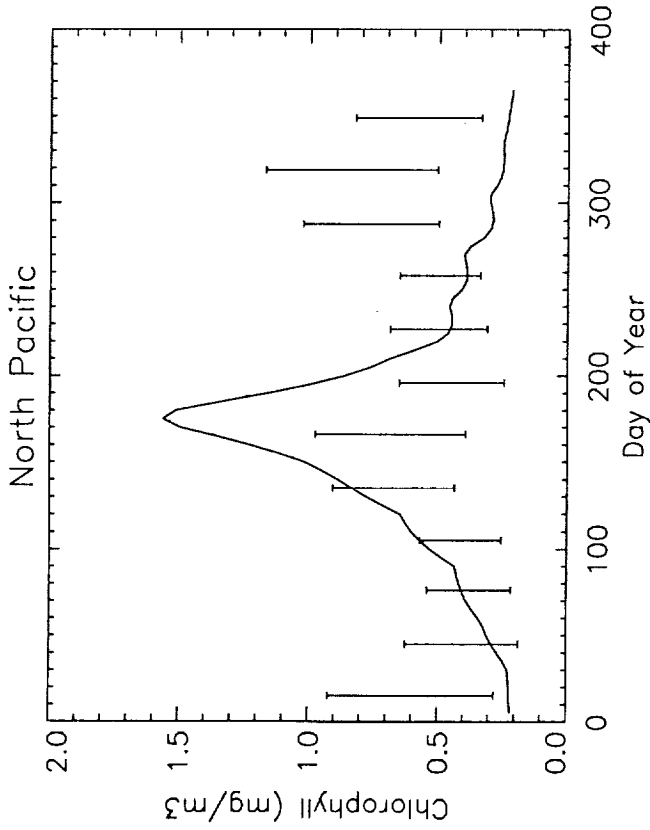
PP

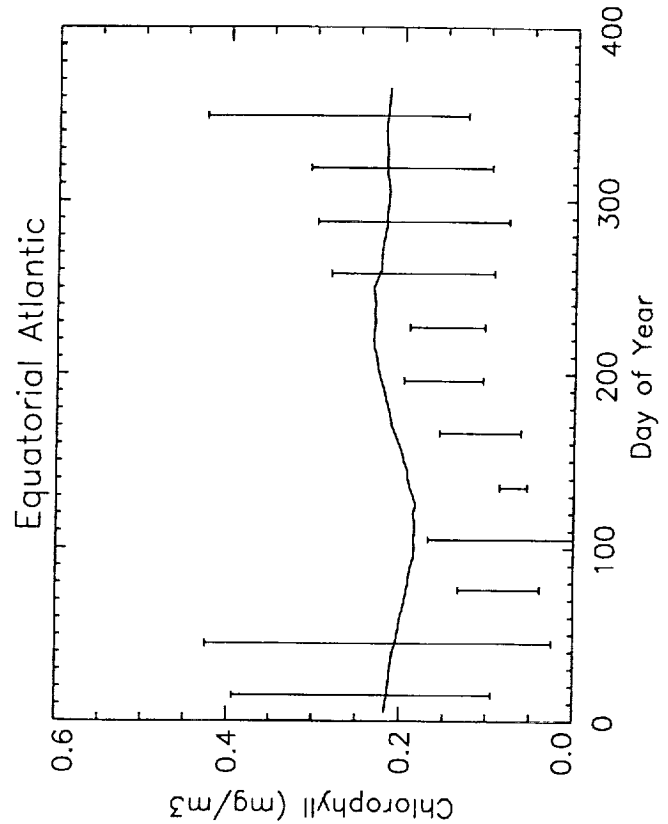
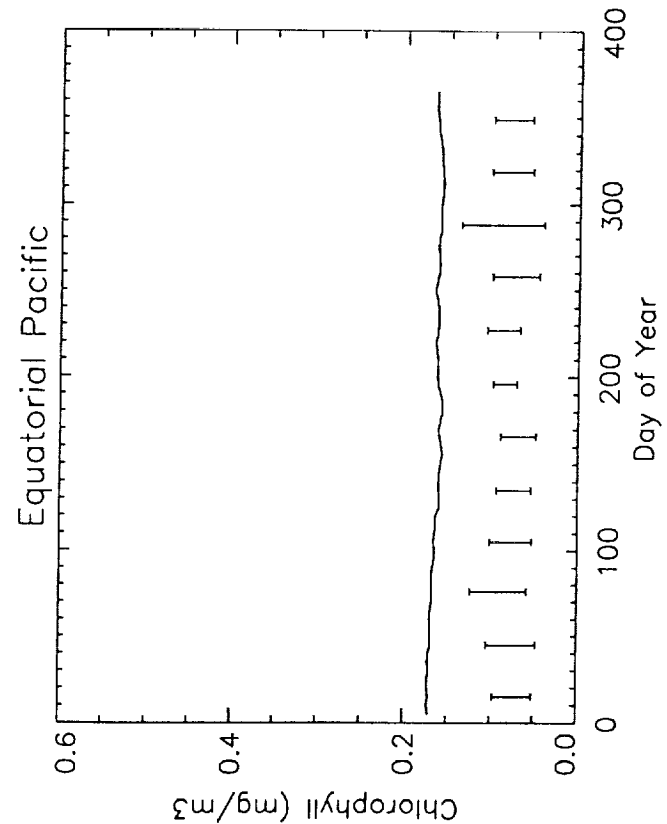
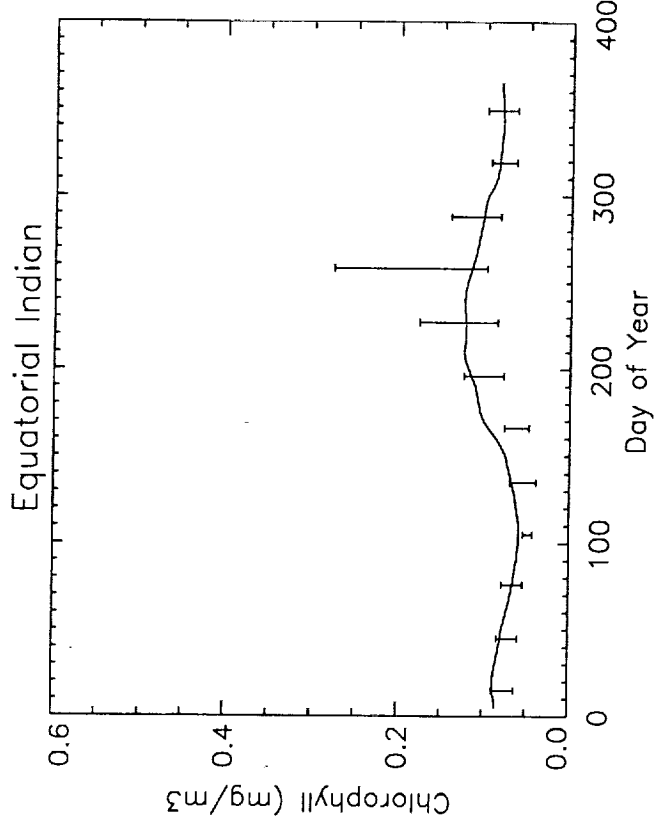
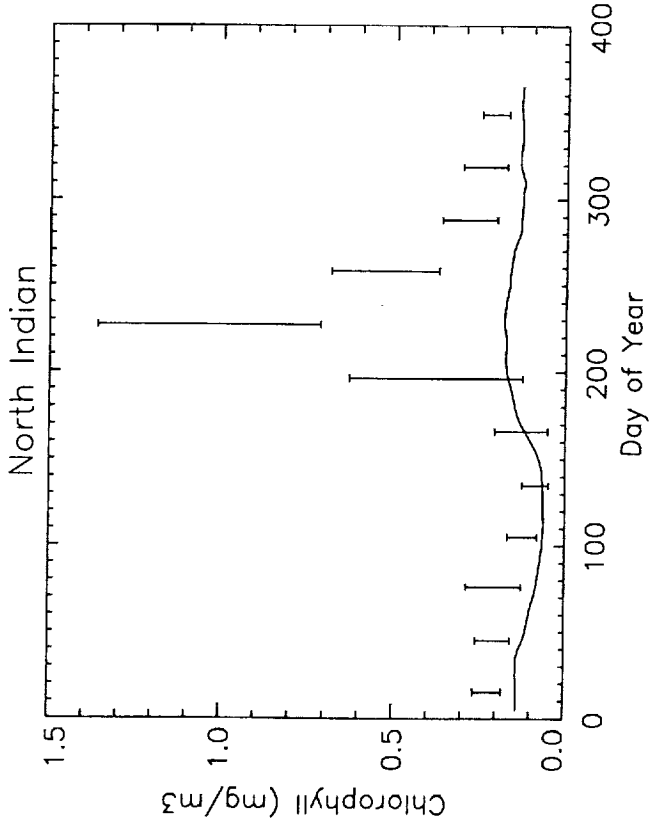
ChlorophyllII, Nutrients

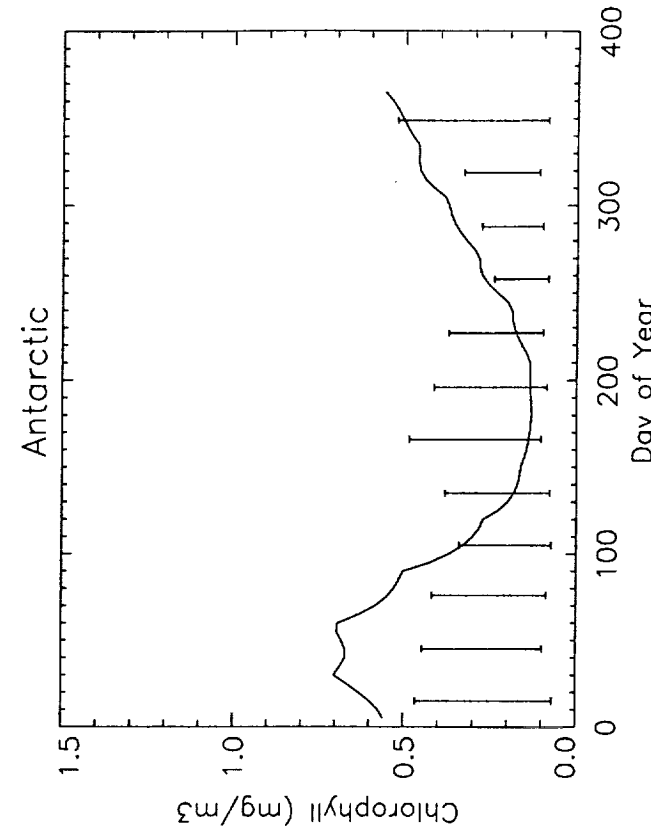
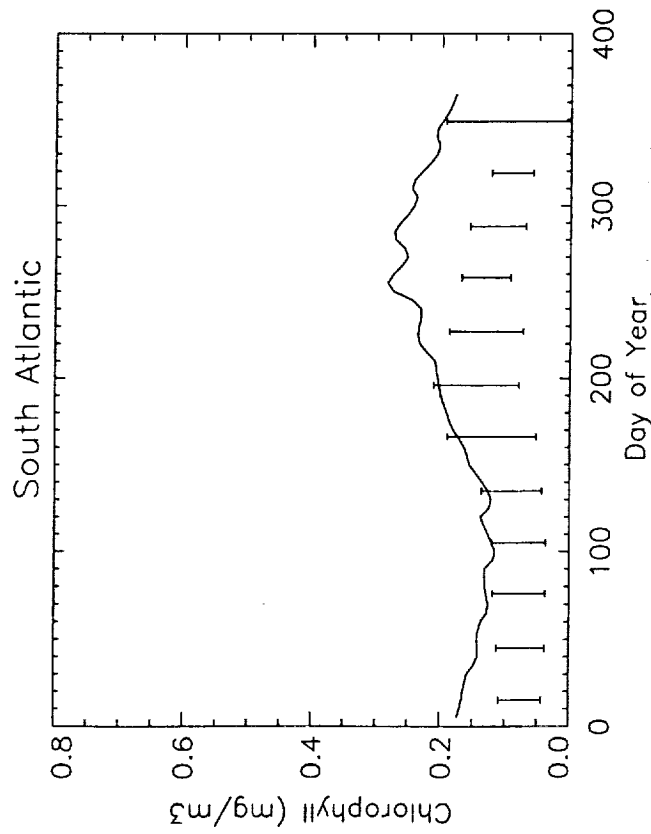
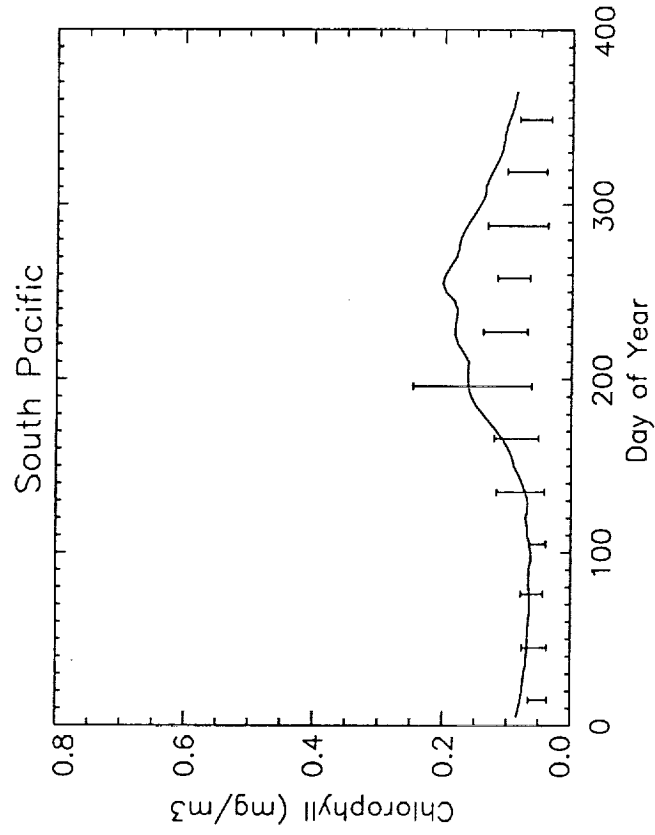
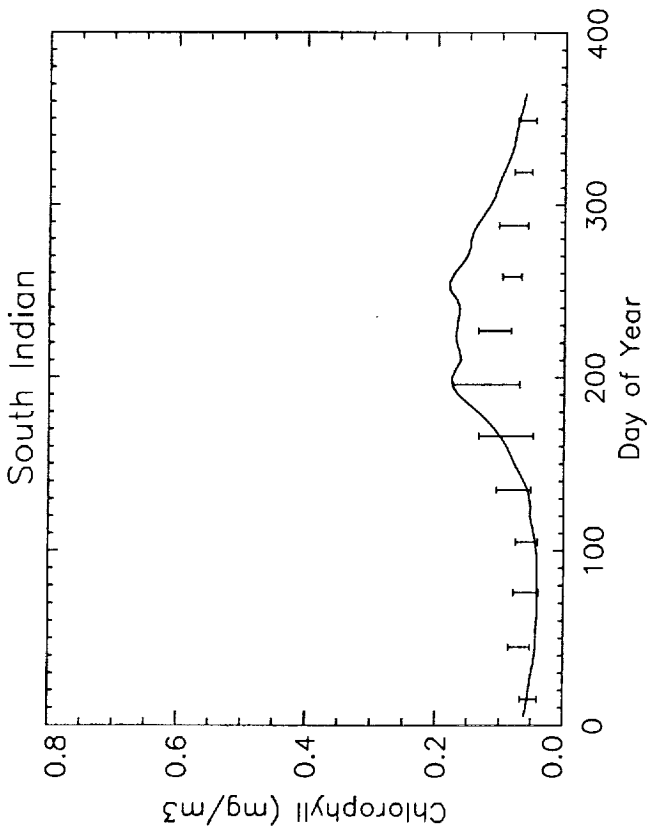
Biochemical Model







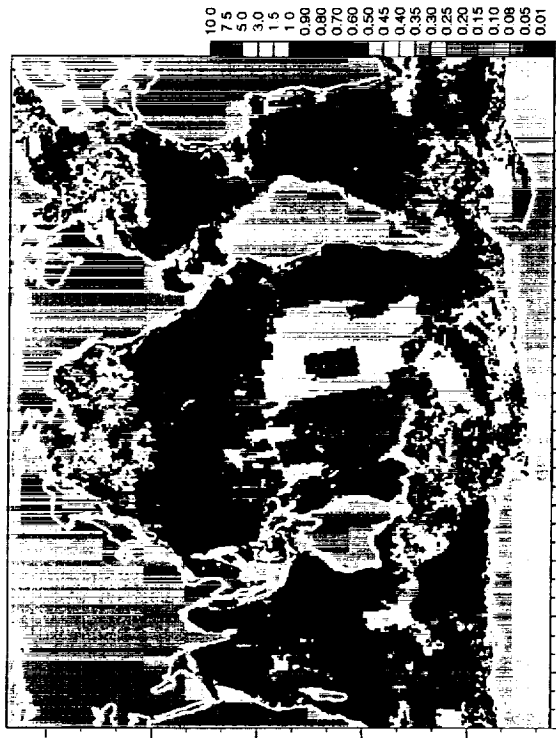




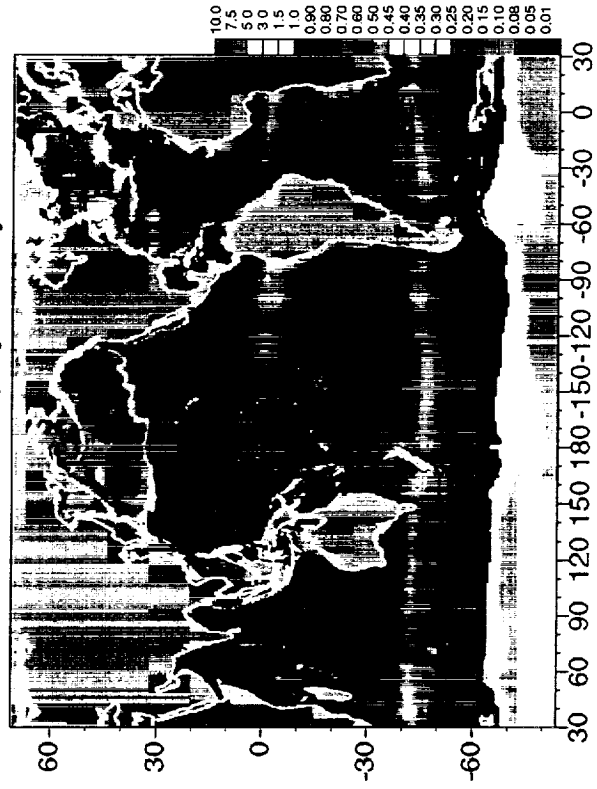
Model Chlorophyll; March



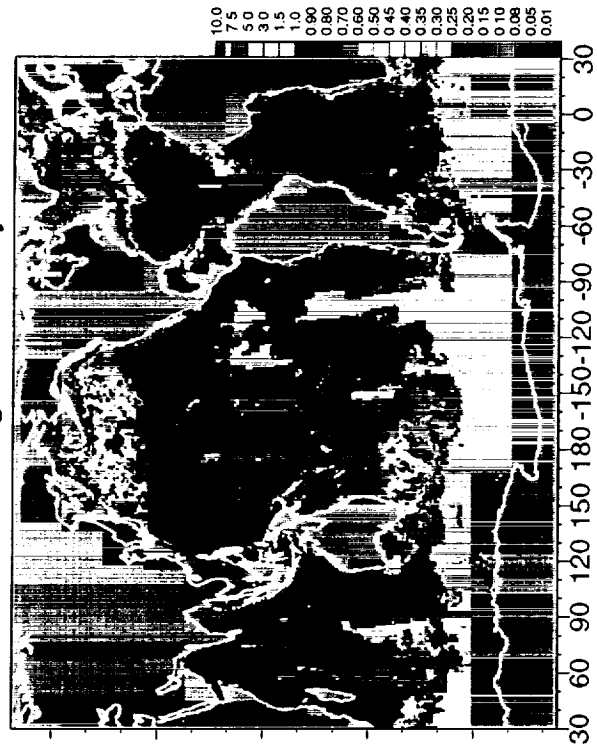
CZCS Pigment; March



Model Chlorophyll; May



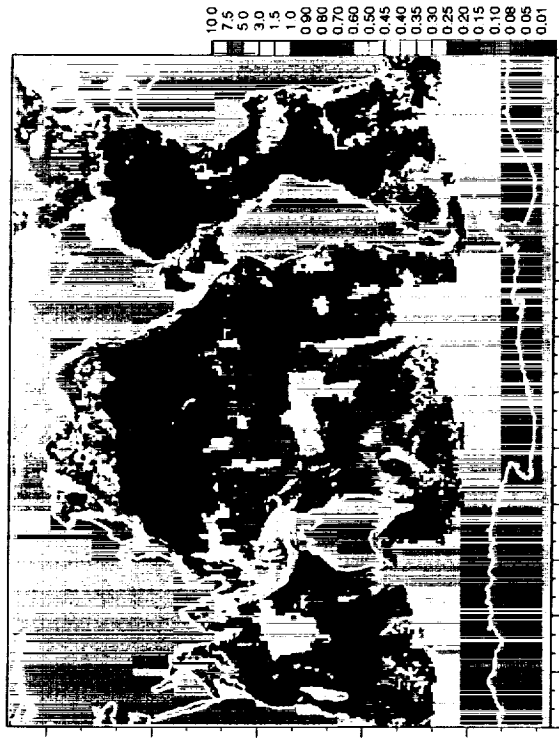
CZCS Pigment; May



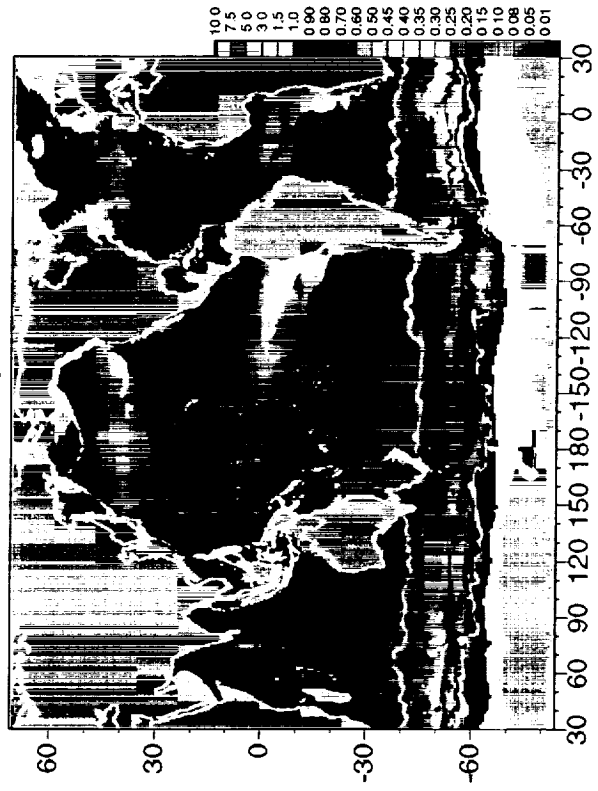
Model Chlorophyll; August



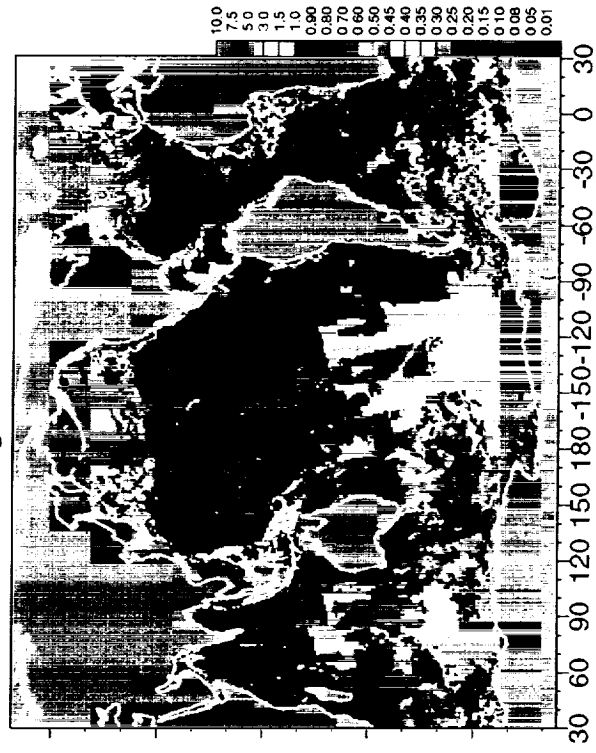
CZCS Pigment; August



Model Chlorophyll; December



CZCS Pigment; December



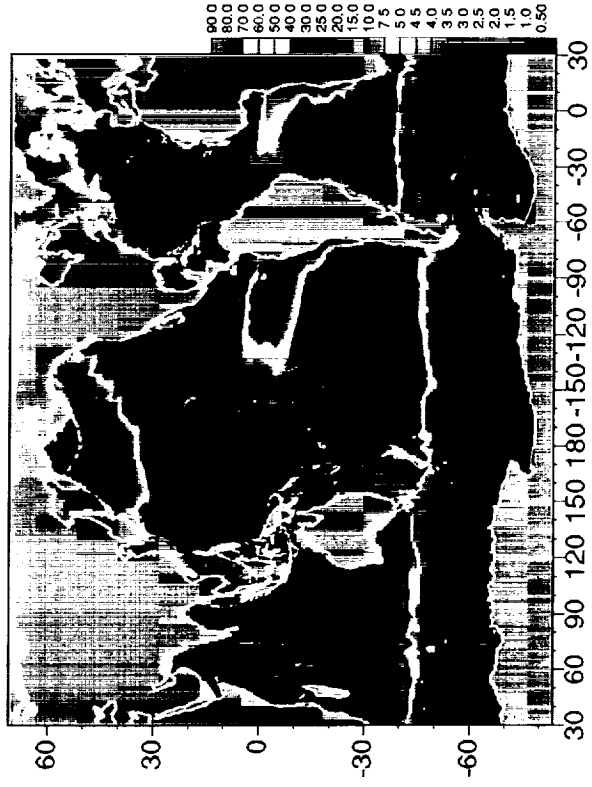
Model Nitrate ; Winter



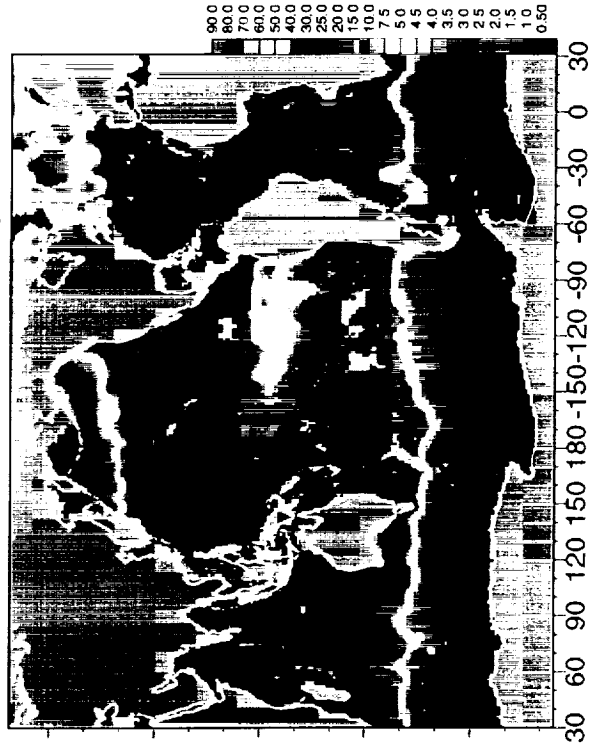
NOAA Nitrate ; Winter



Model Nitrate ; Spring



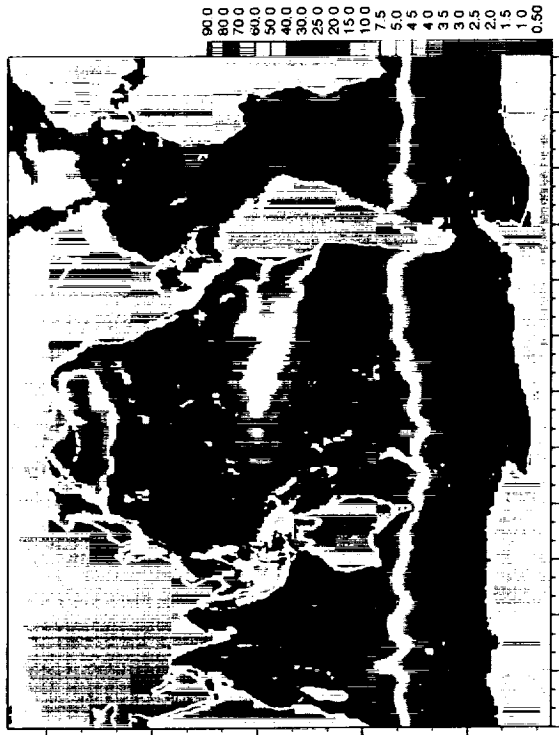
NOAA Nitrate ; Spring



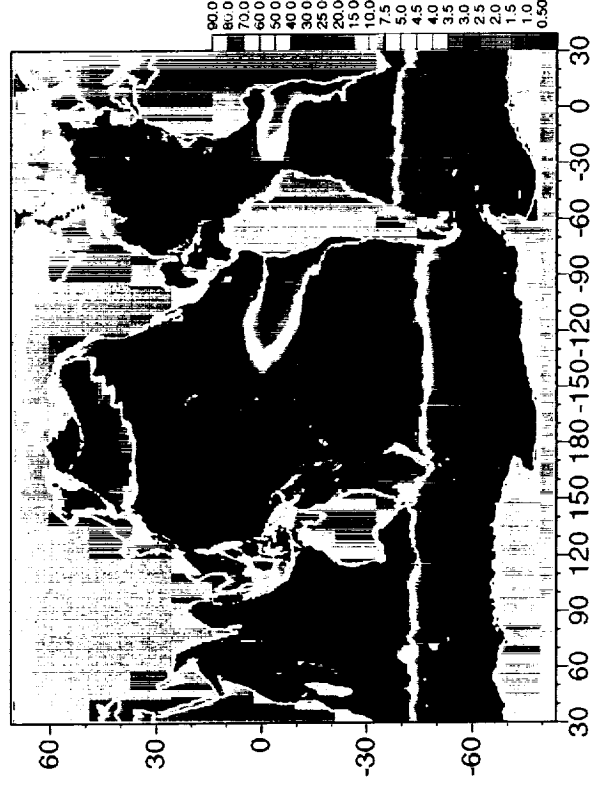
Model Nitrate ; Summer



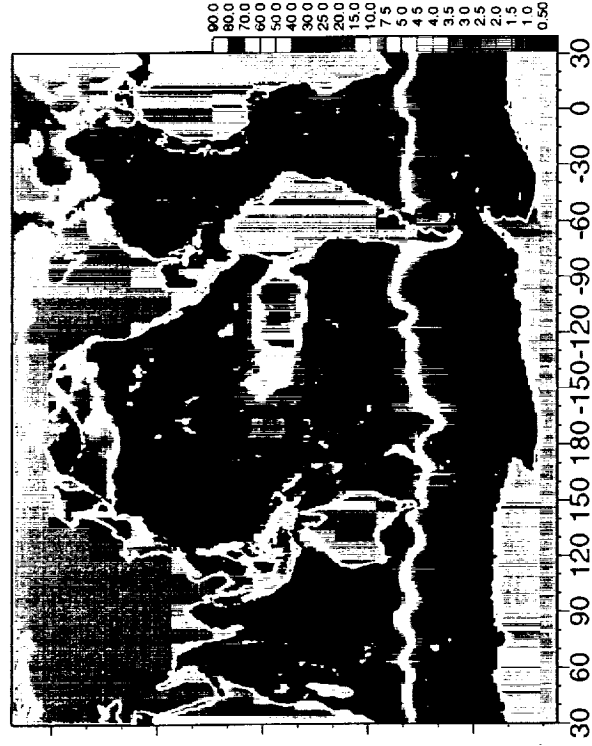
NOAA Nitrate ; Summer



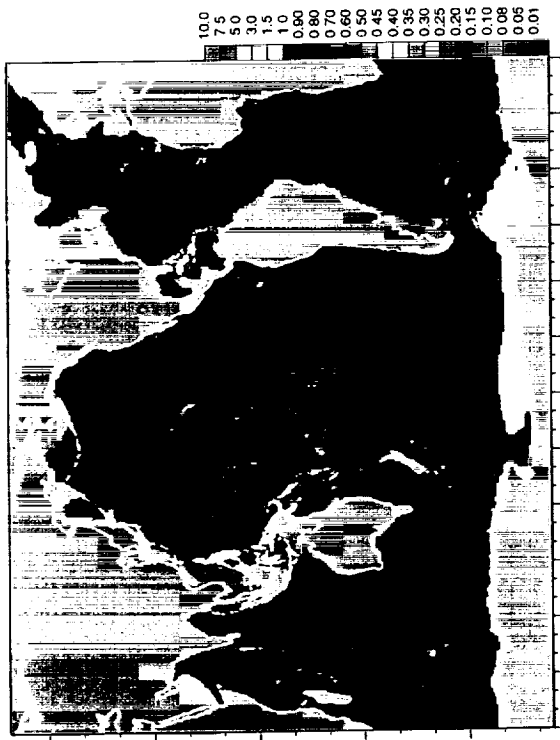
Model Nitrate ; Autumn



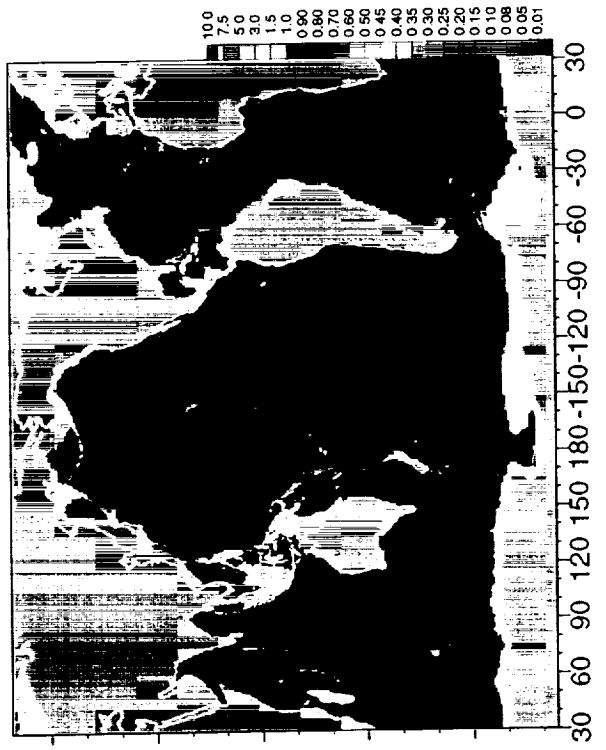
NOAA Nitrate ; Autumn



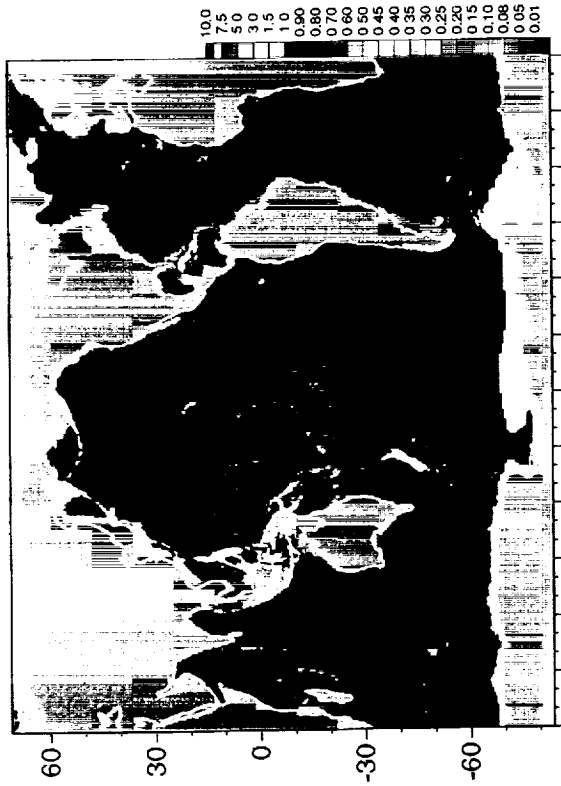
Chlorophytes Initial



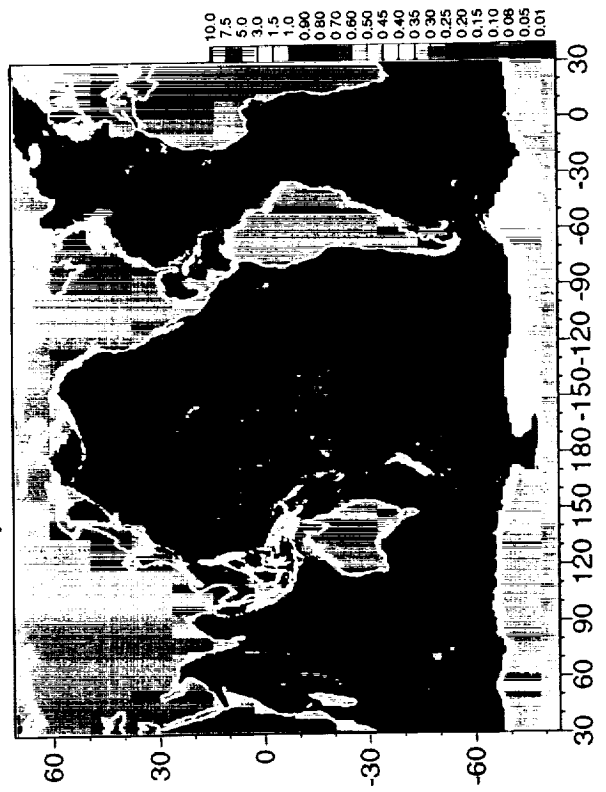
Total Chlorophyll Initial



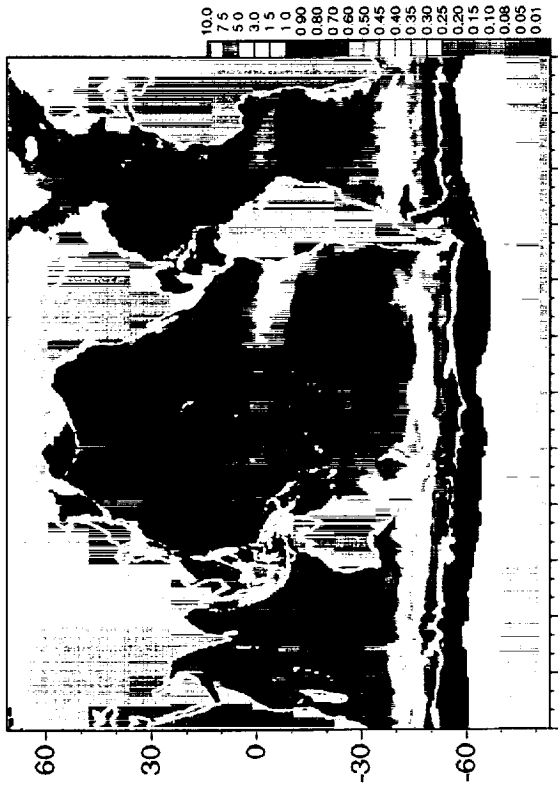
Diatoms Initial



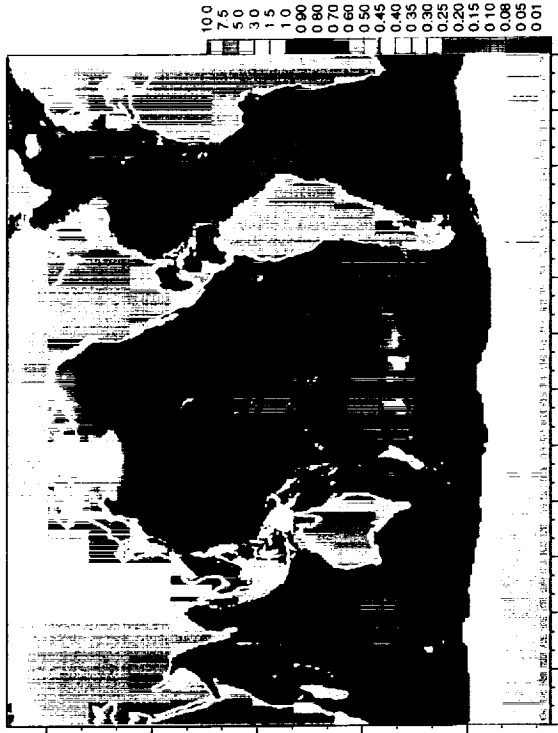
Picoplankton Initial



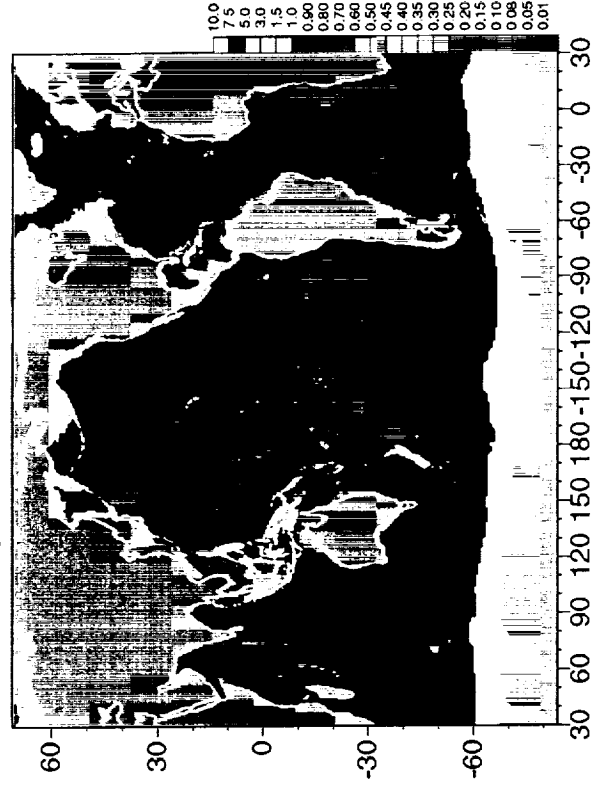
Diatoms October



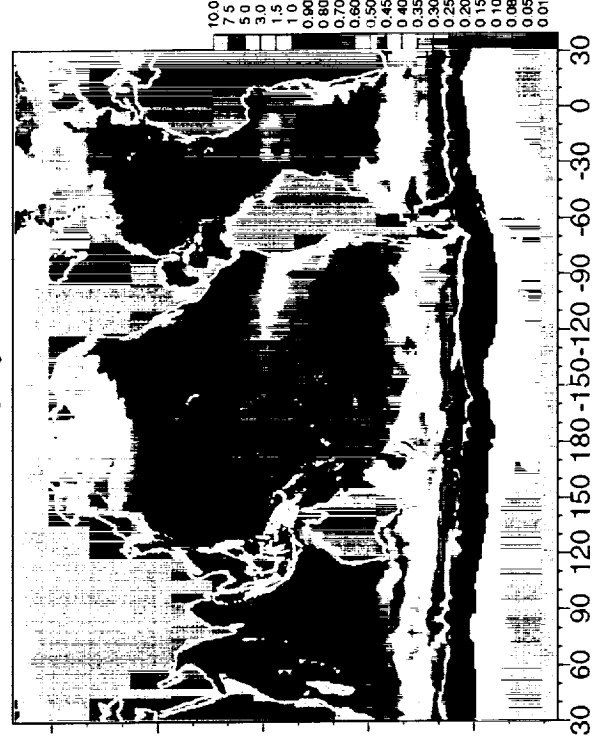
Chlorophytes October



Picoplankton October



Total Chlorophyll October



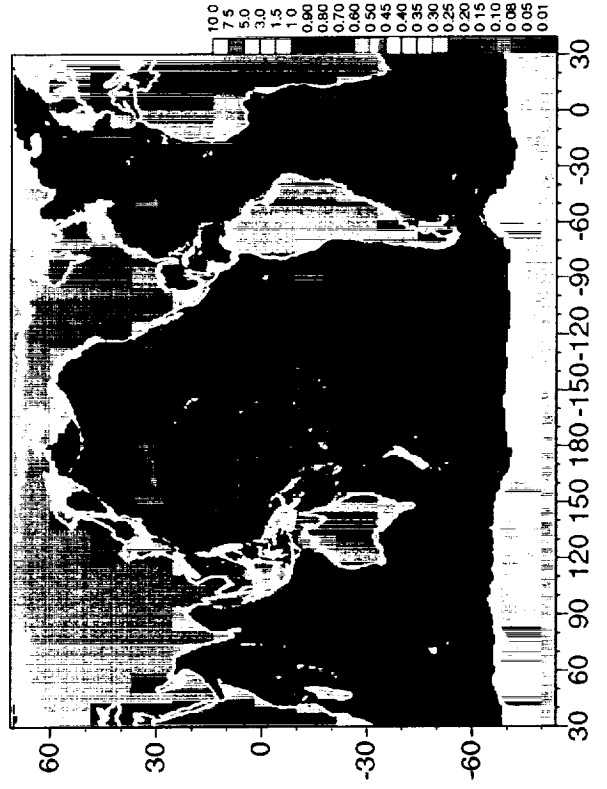
Diatoms April



Chlorophytes April



Picoplankton April



Total Chlorophyll April

